



Dual electron microregion with oxygen vacancy of Fe_{0.8}La/MCM-48 in bridging peracetic acid and ozonation: Taking the pathway of free radical or nonradical generation?

Fengling Pan, Shuhan Fu, Yuhui Wang, Yixiao Zou, Tingting Zhang, Shangyi Li*

Department of Environmental Science and Engineering, College of Chemical Engineering, Beijing University of Chemical Technology, Beijing 100029, China

ARTICLE INFO

Keywords:

Fe_{0.8}La/MCM-48
Surface adsorbed atomic oxygen
O₃/Peracetic acid
¹O₂ generation
Tetracycline hydrochloride degradation

ABSTRACT

Efficient tetracycline hydrochloride (TCH) degradation and interface reaction mechanism were investigated by constructing nonradical pathways in heterogeneous peracetic acid coupling with ozonation (O₃/PAA) process. Ball-milling assisted Fe–La anchoring MCM-48 catalysts with dual electron microregion was designed to trigger ¹O₂-dominated non-radical for strong immunity to environment interference. Results exhibited that 83.4% degradation efficiency of TCH was achieved by Fe_{0.8}La/MCM-48/O₃/PAA system in only 2 min and 94% TCH was degraded in a 12-hour continuous flow experiment. La with oxygen vacancy regulated the local atomic environment and electron structure of Fe sites, which could initiate peracetic acid activation to promote ¹O₂ production by surface adsorbed atomic oxygen (*O_{ad}) reaction and this process overcame a lower reaction energy barrier than the binding of surface *O_{ad} to O₃. This work offers a reasonable interpretation for Fe–La synergy for inducing non-free radical route, which furnishes theoretical support and practical application for heterogeneous O₃/PAA.

1. Introduction

Advanced peroxone process as an emerging technology by O₃ and peroxides coupling has attracted extensive attention and application owing to the obvious synergistic effects in the elimination of recalcitrant contaminants from water and organic synthesis [1–3]. The activity of the process mainly comes from the formed reactive oxygen species (ROS) including sulfate radicals (SO₄^{•−}) in O₃/PDS or O₃/PMS, hydroxyl radicals (*OH), single oxygen (¹O₂) and superoxide radicals (O₂^{•−}) in O₃/H₂O₂ along with the peroxide bond (O–O) breakage in the persulfate structure [4–6]. Normally, enhancing O₃ and peroxides utilizing for ROS generation was considered as the main route for destruction of organic pollutants due to their obviously higher oxidation potential (1.80–2.70 V for *OH and 2.50–3.10 V for SO₄^{•−}) [7]. Thus, heterogeneous catalytic as the interface during O₃/H₂O₂ and O₃/PS process have broad application prospects, which significantly increased ROS yields and higher exposure [8,9]. Notably, it was found that heterogeneous O₃/H₂O₂ and O₃/PS process are dominated by the free radical pathway. Unfortunately, the free radical reactions are susceptible to pH and water matrix, which limited their application in wastewater treatment [10]. Generally, free radicals after reacting with existing anions or humic

acids in water would lead to the generation of lower redox potentials species.

To solve this problem, an increasing number of studies have found that nonradical pathways [e.g., electron-transfer pathway, singlet oxygen (¹O₂) and high-valent metal-oxo species] gained more attention due to better resistance against actual water substrate owing to their moderate redox potentials [11–13]. Wherein, ¹O₂ is a common and effective non-radical, which has a mild redox capacity (2.2 V vs NHE), a relatively long lifetime (2 μs) and a high selectivity due to unoccupied π* orbitals [14]. Therefore, the ¹O₂-dominated peroxone process with excellent resistance to environmental substrate interference has more potential for application in wastewater treatment [15,16]. However, it is still a challenge to promote ¹O₂ production in synergistic ozonation process. In recent years, peroxyacetic acid (PAA) as an important peroxide has shown the advantages of high oxidizing efficiency, less formation of toxic disinfection byproducts and high thermodynamic activation potential [17]. Compared to conventional oxidants such as H₂O₂ and PMS, PAA is more easily activated [18]. In Fan et al.'s research, it emphasized that ¹O₂ could play an important role in the non-radical processes during PAA activation [19]. Additionally, PAA could be activated by high microwave-responsive cobalt-substituted manganese ferrite to form

* Corresponding author.

E-mail address: lishangyi@mail.buct.edu.cn (S. Li).

<https://doi.org/10.1016/j.apcatb.2024.124185>

Received 20 February 2024; Received in revised form 4 May 2024; Accepted 8 May 2024

Available online 11 May 2024

0926-3373/© 2024 Elsevier B.V. All rights reserved, including those for text and data mining, AI training, and similar technologies.

$^1\text{O}_2$ -dominated ROS [20]. Meanwhile, the MnN_4 sites coordinated to pyridine N exhibited a high tendency to decompose O_3 into $^1\text{O}_2$ [21]. Therefore, the $^1\text{O}_2$ -dominated non-radical pathway was expected to be formed in the O_3/PAA process. To further improve the selectivity of $^1\text{O}_2$ generation, it is of great significance to rationally regulate the active sites of the catalysts to promote the high-efficiency formation of the $^1\text{O}_2$.

Namely, to achieve “ $^1\text{O}_2$ -dominated non-radical pathway” strategy in advanced peroxone process, could the specialty designed catalysts help to overcome such a drawback of the limited generation efficiency and enhance emerging contaminants degradation on the interface of solid-gas-liquid three phase in the meantime? A few researches of $^1\text{O}_2$ -dominated catalysis have also been reported in Fe catalysis [22,23]. Iron oxide is a catalyst with advantages of environmental protection and stability. However, the poor electrical conductivity limited its application in catalysis, especially in the free and non-free radicals based Fe_2O_3 -catalytic reaction process [24]. Additionally, it is difficult to selectively generate $^1\text{O}_2$ in the process of iron oxide catalysis. It is reported that the selectivity of $^1\text{O}_2$ generation was closely related to the electronic structure of the active site on the catalyst [24]. In this case, defect engineering became an effective strategy for regulating electronic structures of catalysts to promote $^1\text{O}_2$ generation [25]. For example, the introduction of sulfur defects regulated the d -band centers of the Co-3d orbitals, which promoted the formation of the key intermediate surface adsorbed atomic oxygen ($^*\text{O}_{\text{ad}}$), improving the selectivity of $^1\text{O}_2$ generation [14]. In the meanwhile, Qin et al. reported that $\alpha\text{-Fe}_2\text{O}_3$ with oxygen-rich defects could activate PMS to achieve a $^1\text{O}_2$ -dominated non-radical pathway [26]. Notably, metal doping promoted the production of oxygen defects on Fe_2O_3 and the synergistic effect of dual metal oxides would enhance the peroxone process by improved electron transfer and target substance adsorption [21,24]. To achieve this goal, Lanthanum was chosen as the co-catalyst with the potential advantages of adjusting the crystal structure, increasing the number of active sites, and providing additional reactive oxygen species [27]. More importantly, La as a dopant significantly improved the production of defects and regulated the chemical structure of catalysts [28]. However, the research focus on the effect of La doping the electronic structure of Fe_2O_3 was still a blank about whether this unique modification would selectively generate $^1\text{O}_2$ for enhancing pollutants removal.

In the present study, we for the first time discovered the involvement of interface $^1\text{O}_2$ -dominated ROS in O_3/PAA activation by $\text{Fe}_{0.8}\text{La}/\text{MCM-48}$. This catalyst with oxygen defects and electron-deficient sites was prepared by ball milling and calcination using as-made MCM-48 with high specific surface area as a support. In this synthesis, the confined space was kept between CTAB (Cetyltrimethylammonium bromide) and TEOS (Tetraethyl orthosilicate) for metal loading. Various experiments were conducted to explore the outstanding degradation performance of tetracycline hydrochloride (TCH) as the targeted contaminant. Meanwhile, the promotion effects of on the activity and the physicochemical properties of $\text{Fe}_{0.8}\text{La}/\text{MCM-48}$ were analyzed through advanced in-situ characterization and synchrotron-based X-ray absorption spectroscopy (XAS). Furthermore, density functional theory (DFT) calculation was carried out to quantify optimized potential free energy diagrams and elucidate the strengthening mechanism of surface $^*\text{O}_{\text{ad}}$ bonding with PAA at the molecular level. Additionally, the role of Fe–La synergistic effect in expediting the electronic structure regulation and oxygen vacancy to achieve the efficient conversion of $^1\text{O}_2$ was deeply investigated. This study reveals intricate insights into the active sites and O_3/PAA activation mechanism on $\text{Fe}_{0.8}\text{La}/\text{MCM-48}$ materials, which could shed light on the structure–property relationships at the solid-liquid-gas three phase interface in peroxone advanced oxidation process.

2. Materials and methods

2.1. Chemicals and reagents

The information of chemical reagents involved in this study was

provided in Text S1.

2.2. Catalysts preparation and characterization

Mesoporous MCM-48 was synthesized by a hydrothermal method according to literature [29]. Briefly, 9.84 g of CTAB as template agent was dissolved in alkaline solution (NaOH, 0.75 M, 70 mL) to yield a homogenous mixture. Then, 15 mL TEOS as silica source was slowly added in the solution under continuous stirring. After stirring at 2°C for 1 h, the above mixture was transferred into a Teflon-lined autoclave at 100°C for 72 h. After cooling down to room temperature, the MCM-48 containing the template agent CTAB was obtained by filtration and dried at 110°C in the oven. Catalysts with 4 wt% metal loading were prepared due to better catalytic performance according to previous study [30]. Therefore, the mixture of $\text{Fe}(\text{NO}_3)_3 \cdot 9\text{H}_2\text{O}$ (0.072 g), La $(\text{NO}_3)_3 \cdot 6\text{H}_2\text{O}$ (0.094 g) and MCM-48 (1 g) was poured into a ball mill (a MITR-YXQM-2 L, China) with a stainless-steel pot (80 mL) and 25 stainless steel balls (10 mm in diameter) at rotational speed and time before calcination. Milling conditions were 60 min at 400 rpm. The mixed powder was transferred to a Muffle furnace for calcination at 500°C for 5 h with a heating rate of $2^\circ\text{C}/\text{min}$. The calcined powder-form catalysts were designated as $\text{Fe}_{0.8}\text{La}/\text{MCM-48}$. And 0.8 represented the molar ratio of Fe/La. Detailed information of catalysts characterization was showed in Text S2.

2.3. Degradation experiments

Batch experiments were generally carried out in 100 mL conical flasks with covers at room temperature under magnetic stirring (250 rpm). Typically, 2.5 mg of catalysts, and a certain amount of 15% PAA solution was dispersed into 43 mL of ultrapure water. Then, 2 mL of saturated ozone water (25 ppm) prepared by the ozone generator (Tonglin, Beijing) was added to trigger the reaction. Immediately, 20 mg/L TCH was designed to simulate high concentration pharmaceutical wastewater [31–33]. A 1.0 mL sample was withdrawn at different time intervals (0, 2, 5, 10, 20 min) from the above mixture, filtered through a single-use $0.22\text{-}\mu\text{m}$ polyamide 66 membrane and quenched with 10 μL of a sodium thiosulfate solution (10 ppm) before analysis. All experiments were performed in triplicate, and the average values of TCH concentrations with standard deviations were presented. The effects of milling time, milling speed, PAA dosages and different initial pH on catalytic performance in $\text{Fe}_{0.8}\text{La}/\text{MCM-48}/\text{O}_3/\text{PAA}$ were investigated. The initial pH value was adjusted using 0.1 M H_2SO_4 and 0.1 M NaOH. In addition, a series of quenchants (e.g., methanol (MeOH), tert-butanol (TBA), chloroform (CF) and furfuryl alcohol (FFA)) were used to clarify the primary and secondary active species. All the catalysts in the cycle experiment were collected after degradation experiment, filtered and washed with ultra-pure water.

2.4. Analysis and calculation

The concentration of different organic compounds was quantified by liquid chromatography (LC, APD-16, Shimadzu) equipped with a Agilent TC-C18(2) ZORBAX SB-C18 ($5\text{ }\mu\text{m}$, $4.6 \times 250\text{ mm}$) column and a UV detector. Detailed detection conditions were listed in Table S1. The O_3 concentration was analyzed by using indigo method [34]. The degradation intermediates of TCH were determined by a liquid chromatography-mass spectrometer (HPLC-MS, Xevo G2 QTOF, Waters Co., USA), equipped with a Thermo Scientific Accucore aQ C18 column ($2.6\text{ }\mu\text{m}$, $2.1\text{ mm} \times 50\text{ mm}$). The mass spectra with electrospray ionization (ESI) source were detected in a positive ionization mode. The capillary voltage was +3500 V, the collision voltage range was 10–40 eV, the ion source temperature was 120°C , and the desolvation temperature was 500°C . High-purity nitrogen and argon were used as the desolvation gas (500 L/h) and collision gas (5 L/h). The ECOSAR software (2.0) was used to evaluate the acute and chronic toxicity of

TCH and its degradation intermediates. The DFT calculation was performed using CASTEP program package. And the detailed was described in Text S3.

3. Results and discussions

3.1. Characterization of catalysts

To fabricate $\text{Fe}_{0.8}\text{La}/\text{MCM-48}$, three-dimensional Si–O skeleton with CTAB surfactant was employed as the precursor through ball milling assisted method to maximize the exposure of active sites as illustrated in Fig. 1a. Meanwhile, the confined space could be obtained between TEOS and CTAB surfactant for metal filling [35]. The scanning electron microscopy (SEM) images in Figure S1 showed the morphologies of $\text{Fe}_{0.8}\text{La}/\text{MCM-48}$, $\text{La}/\text{MCM-48}$ and $\text{Fe}/\text{MCM-48}$. Oxide particles with regular shape and smooth surface were observed on the $\text{Fe}/\text{MCM-48}$. And the as-prepared materials featured 3D spherical structure and the absence of oxide particles on the surface of $\text{La}/\text{MCM-48}$ and $\text{Fe}_{0.8}\text{La}/\text{MCM-48}$ implied their homogeneous distribution on MCM-48. The EDS mapping images showed that Fe and La were evenly distributed on the surface of $\text{Fe}_{0.8}\text{La}/\text{MCM-48}$ (Fig. 1c). The high resolution

transmission electron microscopic (HRTEM) image of $\text{Fe}_{0.8}\text{La}/\text{MCM-48}$ exhibit dispersed and amorphous metal oxide particles, which also confirmed by the SAED pattern (Fig. 1d and Figure S2). In addition, the ratio of Fe/La atoms in $\text{Fe}_{0.8}\text{La}/\text{MCM-48}$ was approximately 1.38, which was detected by ICP–OES (Table S2). As shown in Fig. 1e, the X-ray diffraction (XRD) pattern of all the catalysts exhibited the wide peaks in the range $15\text{--}35^\circ$ were attributed to the peak of amorphous SiO_2 of MCM-48. For $\text{Fe}/\text{MCM-48}$, the diffraction peaks located at 24.1° , 33.2° , 35.6° , 40.8° , 49.5° , 54.0° , 62.4° and 63.9° were corresponded to (012), (104), (110), (113), (024), (116), (214) and (300) crystal planes of Fe_2O_3 (PDF#99–0060), which was consistent with the results of SEM image. No obvious PXRD diffraction peaks of $\text{Fe}_{0.8}\text{La}/\text{MCM-48}$ could be observed, implying that the presence of La as the amorphous substance would make Fe species on the $\text{Fe}_{0.8}\text{La}/\text{MCM-48}$ be highly dispersed and present as amorphous Fe_2O_3 [36]. According to Fig. 1c, the uniform distribution of Fe and La suggested that La as the amorphous substance may be doped into Fe_2O_3 .

Figure S3 exhibited the N_2 adsorption–desorption isotherms of $\text{Fe}_{0.8}\text{La}/\text{MCM-48}$, $\text{La}/\text{MCM-48}$ and $\text{Fe}/\text{MCM-48}$. All the samples displayed a reversible type IV isotherm and one hysteresis loop, which is the characteristic of mesoporous materials [37]. According to

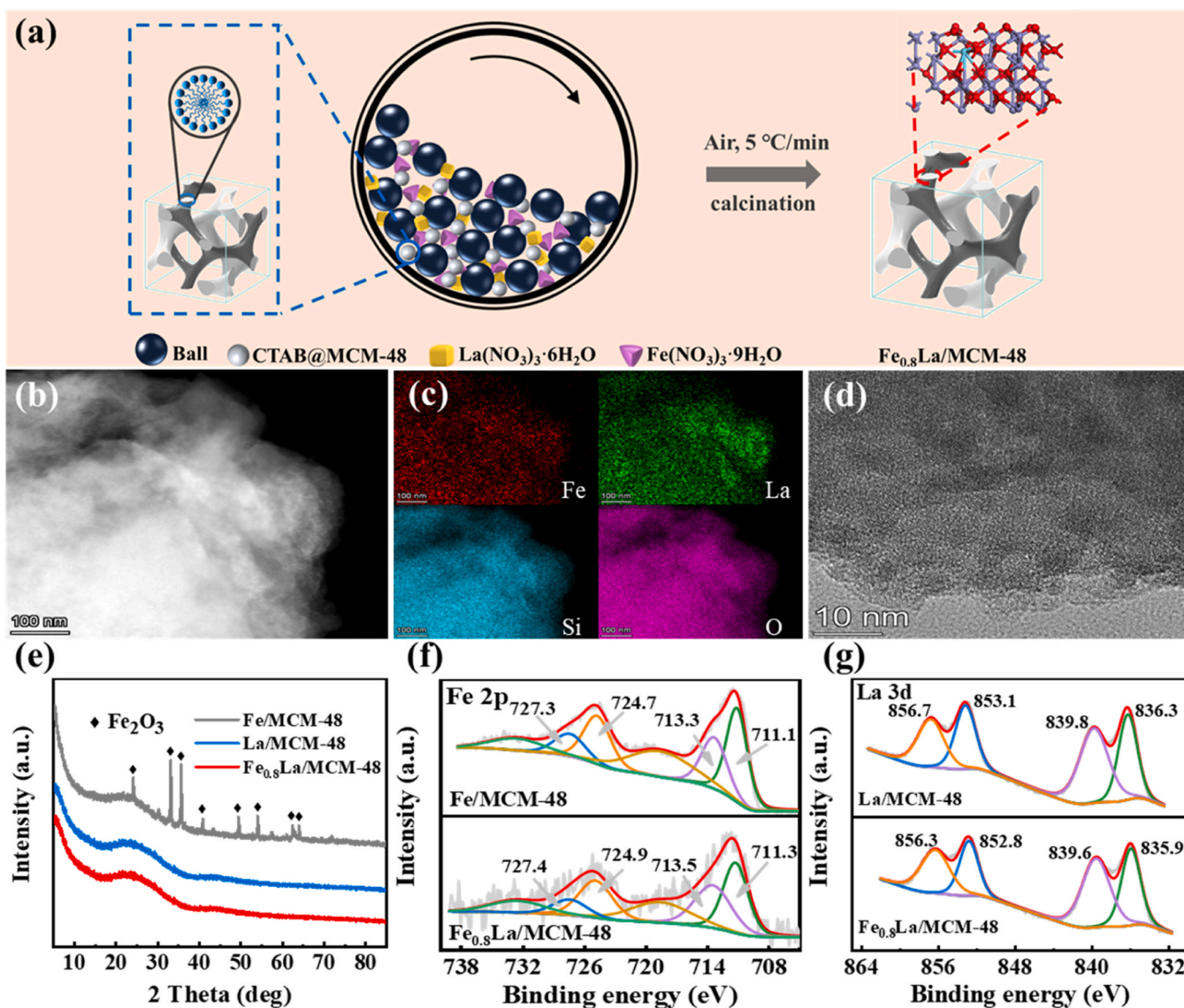


Fig. 1. (a) Schematic diagram of the samples fabrication; (b) HAADF-STEM image and (c) corresponding EDS mapping results of $\text{Fe}_{0.8}\text{La}/\text{MCM-48}$; (d) TEM image of $\text{Fe}_{0.8}\text{La}/\text{MCM-48}$; (e) XRD diffraction patterns of all samples; (f) Fe 2p and (g) La 3d XPS spectra.

Figure S3b, the samples were locating in the range of mesoporous. Compared with other samples, Fe/MCM-48 displayed much lower specific surface area ($830 \text{ m}^2/\text{g}$), attributing to the deposition of Fe_2O_3 particles within the mesoporous channels and causing pore blockage (Table S3). La may be beneficial to inhibit the deposition of oxide particles to block the pores due to the highest specific surface area of La/MCM-48. Although the mesoporous channels of $\text{Fe}_{0.8}\text{La}/\text{MCM-48}$ were occupied by oxide particles, it still had satisfactory specific surface area ($911 \text{ m}^2/\text{g}$) and pore diameter (2–6 nm). The presence of iron and lanthanum in the $\text{Fe}_{0.8}\text{La}/\text{MCM-48}$ was verified by wide scan spectra of X-ray photoelectron spectroscopy (XPS) (Figure S4a). In Fig. 1f of high-resolution spectra of Fe 2p, the Fe $2p_{1/2}$ peak at 724.7 eV and the Fe $2p_{3/2}$ peak at 711.1 eV were attributed to Fe(II), and the Fe $2p_{1/2}$ peak at 727.3 eV and the Fe $2p_{3/2}$ peak at 713.3 eV were assigned to Fe(III) [38,39]. Compared with Fe/MCM-48, the peaks in $\text{Fe}_{0.8}\text{La}/\text{MCM-48}$ slightly moved to high binding energy, suggesting a change in the electronic structure of Fe cations. As for the La 3d XPS spectra of La/MCM-48, four pairs of La $3d_{5/2}$ and La $3d_{3/2}$ peaks appeared at 836.3, 839.8, 853.1 and 856.7 eV, in which the peaks at 839.8 eV and 856.7 eV were assigned to satellite peaks (Fig. 1g) [40]. The peaks of La $3d_{5/2}$ and La $3d_{3/2}$ slightly shifted toward lower binding energy after the introduction of Fe, which could be attributed to the elevated electron density around La cations. Thus, the shift in the binding energies of $\text{Fe}_{0.8}\text{La}/\text{MCM-48}$ indicated the existence of electronic interaction between Fe and La, which modulated the electronic environments of Fe cations [41]. The XPS spectra of O 1s can be deconvoluted into three distinct peaks (Figure S4b). The peaks at ~ 531.5 eV, ~ 532.6 eV and ~ 533.3 eV correspond to the oxygen vacancies, surface hydroxyls (–OH) and Si–O bond, respectively [42,43]. The presence of electron

paramagnetic resonance (EPR) signal at $g \sim 2.04$ on the sample was attributed to oxygen vacancies, which further confirmed the presence of oxygen vacancies (Fig. 2a) [44]. $\text{Fe}_{0.8}\text{La}/\text{MCM-48}$ has the highest content of oxygen vacancies, suggesting that La doping promoted the generation of oxygen vacancies.

To further investigate the chemical state and coordination environment of $\text{Fe}_{0.8}\text{La}/\text{MCM-48}$, X-ray absorption fine structure spectroscopy (XAFS) analyses were performed. In Fig. 2b. The absorption edge of $\text{Fe}_{0.8}\text{La}/\text{MCM-48}$ shifted toward a higher binding energy compared with that of Fe_2O_3 , which revealed that the valence state of Fe increases toward Fe(III). The Fe K-edge Fourier transform extended X-ray absorption fine structures (FT-EXAFS) curve of $\text{Fe}_{0.8}\text{La}/\text{MCM-48}$ indicated a conspicuous peak at 1.88 \AA , which corresponded to shorter Fe–O chemical bond than that in Fe_2O_3 ($\approx 1.98 \text{ \AA}$) and Fe_3O_4 ($\approx 1.91 \text{ \AA}$) (Fig. 2c). These results indicated that the introduction of La regulated the local atomic environment of Fe sites in $\text{Fe}_{0.8}\text{La}/\text{MCM-48}$. Further FT-EXAFS fitting in K-space and R-space were performed to explore the local coordination environment of Fe sites in $\text{Fe}_{0.8}\text{La}/\text{MCM-48}$ (Fig. 2d and Figure S5). The fitting information is shown in Table 1. The results suggested the presence of Fe–Fe ($R=3.64 \text{ \AA}$, $\text{CN}=1.3$) and Fe–La shells ($R=2.77 \text{ \AA}$, $\text{CN}=1.5$) except Fe–O shells ($R=1.88 \text{ \AA}$ and $\text{CN}=5.2$). The distances of Fe–Fe bond and Fe–La bond were longer than 2 \AA , suggesting that Fe–Fe and Fe–La were located at the second shell. In addition, the Fe–O coordination number of $\text{Fe}_{0.8}\text{La}/\text{MCM-48}$ decreased from 6.0 to 5.2 compared to that of Fe_2O_3 , indicating the existence of oxygen vacancies changed the coordination of chemical bonds [45]. The wavelet transform (WT) analysis on k^2 -weighted EXAFS showed the difference in coordination environment around Fe atoms in $\text{Fe}_{0.8}\text{La}/\text{MCM-48}$ (Fig. 2e). The results revealed that Fe–O–La structure and oxygen

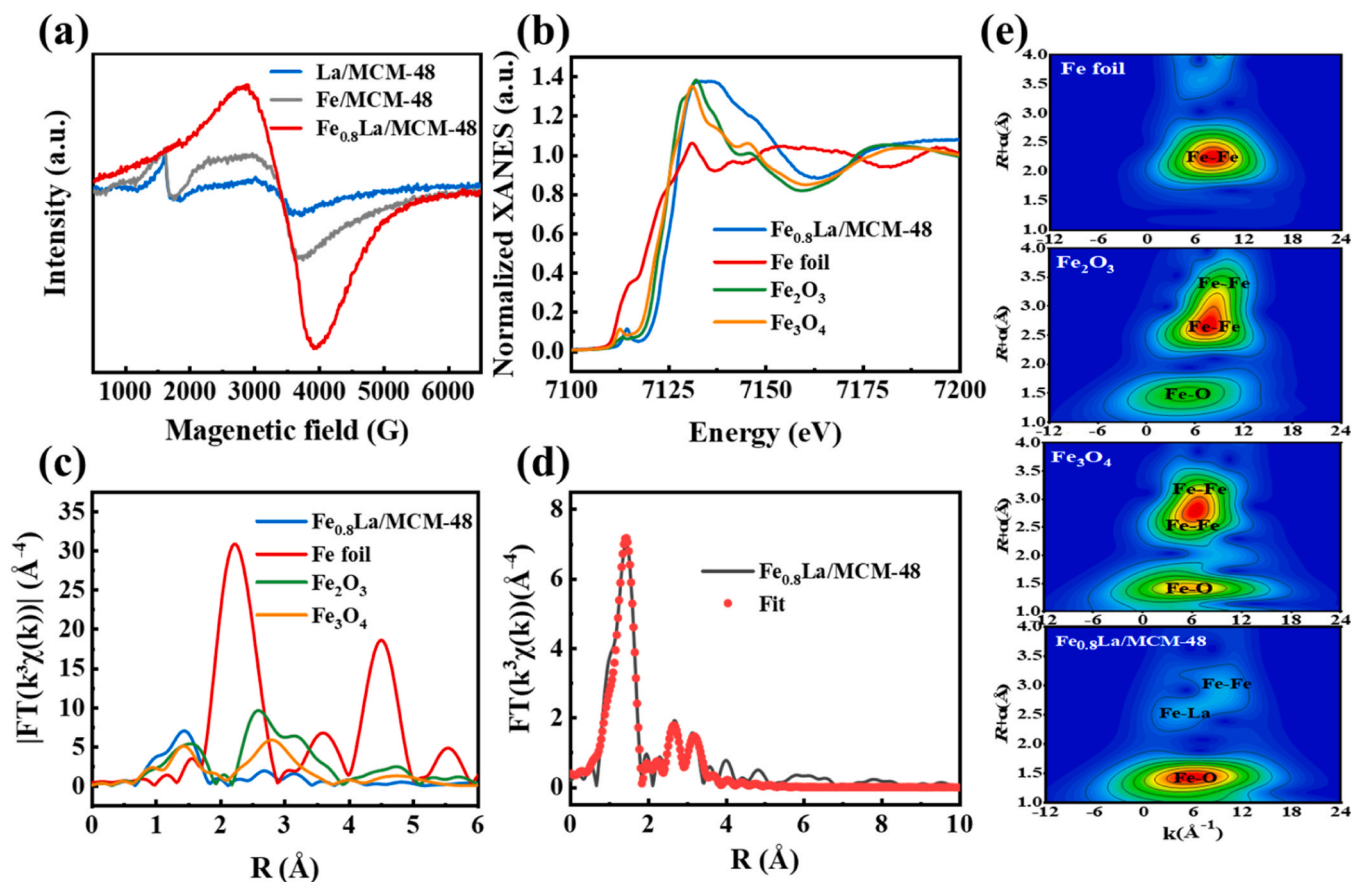


Fig. 2. (a) EPR spectra of La/MCM-48, Fe/MCM-48 and $\text{Fe}_{0.8}\text{La}/\text{MCM-48}$; (b) Fe K-edge XANES spectra of $\text{Fe}_{0.8}\text{La}/\text{MCM-48}$ and reference samples; (c) Fourier transform at the Fe K-edge of $\text{Fe}_{0.8}\text{La}/\text{MCM-48}$ and reference samples; (d) EXAFS fitting result of $\text{Fe}_{0.8}\text{La}/\text{MCM-48}$ in R space; (e) Wavelet transform of Fe foil, Fe_2O_3 , Fe_3O_4 and $\text{Fe}_{0.8}\text{La}/\text{MCM-48}$.

Table 1EXAFS fitting parameters at the Fe *K*-edge for various samples.

Sample	Shell	CN ^a	R(Å) ^b	$\sigma^2(\text{\AA}^2)^c$	$\Delta E_0(\text{eV})^d$	R factor
Fe-foil	Fe-Fe	8*	2.462±0.018	0.0050	5.1	0.0061
	Fe-Fe	6*	2.843±0.023	0.0050	4.5	
Fe ₂ O ₃	Fe-O	6.0	1.981±0.003	0.0129	-1.7	0.0027
	Fe-Fe	6.2	2.985±0.002	0.0082	3.5	
Fe ₃ O ₄	Fe-Fe	2.6	3.656±0.003	0.0014	-8.7	0.0023
	Fe-O	2.9	1.912±0.005	0.0030	3.4	
	Fe-O	2.3	2.090±0.007			
	Fe-Fe	18.9	3.082±0.003	0.0233	6.4	
	Fe-Fe	16.6	3.487±0.005			
	Fe-O	5.2	1.883±0.003	0.0074	-3.1	
Fe _{0.8} La/MCM-48	Fe-O	5.2	1.883±0.003	0.0074	-3.1	0.0079
	Fe-La	1.5	2.775±0.014	0.0125	12.9	
	Fe-Fe	1.3	3.639±0.018	0.0054	-9.6	
	Fe-Fe	±0.4				

Note:

^a CN, coordination number;^b R, the distance to the neighboring atom;^c σ^2 , the Mean Square Relative Displacement (MSRD);^d ΔE_0 , inner potential correction; R factor indicates the goodness of the fit. S_0^2 was fixed to 0.739, according to the experimental EXAFS fit of Fe foil by fixing CN as the known crystallographic value.^{*} This value was fixed during EXAFS fitting, based on the known structure of Fe.

vacancies regulated the electronic structure of Fe sites.

3.2. Catalytic performance

A series of experiments were performed to assess the catalytic activity of modified MCM-48 (Fe/MCM-48, La/MCM-48 and Fe_{0.8}La/MCM-48) for activating PAA coupling with O₃ by means of TCH degradation (Fig. 3a and Figure S6). La/MCM-48 presented the highest adsorption efficiency of TCH (48.5%), which might be related to the larger specific surface area (1155 m²/g) and the stronger affinity between La and TCH. Previous study reported that La could form stable La-TC inner sphere complexes with TCH by chemisorption [46]. Compared with the Fe/MCM-48 or La/MCM-48 suspension, the Fe_{0.8}La/MCM-48 suspension showed a higher degradation efficiency during the heterogenous PAA and O₃ system, attributing to the synergistic action of Fe and La and higher content of oxygen vacancies. Hence, Fe_{0.8}La/MCM-48 with the best catalytic performance was used in the onward experiments. As shown in Fig. 3b and Figure S7, limited oxidation reaction process occurred in PAA or O₃ alone. 56.6% and 64.4% of TCH could be degraded by Fe_{0.8}La/MCM-48 catalyzing O₃ and PAA, respectively. The degradation efficiency of TCH in the Fe_{0.8}La/MCM-48/PAA system increased slowly when the reaction is in process. Compared with Fe_{0.8}La/MCM-48/PAA system, the degradation efficiency of Fe_{0.8}La/MCM-48/O₃/PAA system was 83.4% in 2 min. This demonstrated a more rapid and efficient degradation performance of the Fe_{0.8}La/MCM-48/O₃/PAA system. Furthermore, 37.1% of TCH can be adsorbed on the Fe_{0.8}La/MCM-48 surface after 20 min, which could be attributed to the higher specific surface area of Fe_{0.8}La/MCM-48 (911 m²/g). Though O₃ and PAA were added to the solution together, the degradation efficiency of TCH was increased slightly up to 41.1% after 20 min due to the inert reaction between O₃ and PAA. In comparison, the introduction of Fe_{0.8}La/MCM-48 into the O₃/PAA system significantly increased the TCH degradation efficiency (96.0%). As

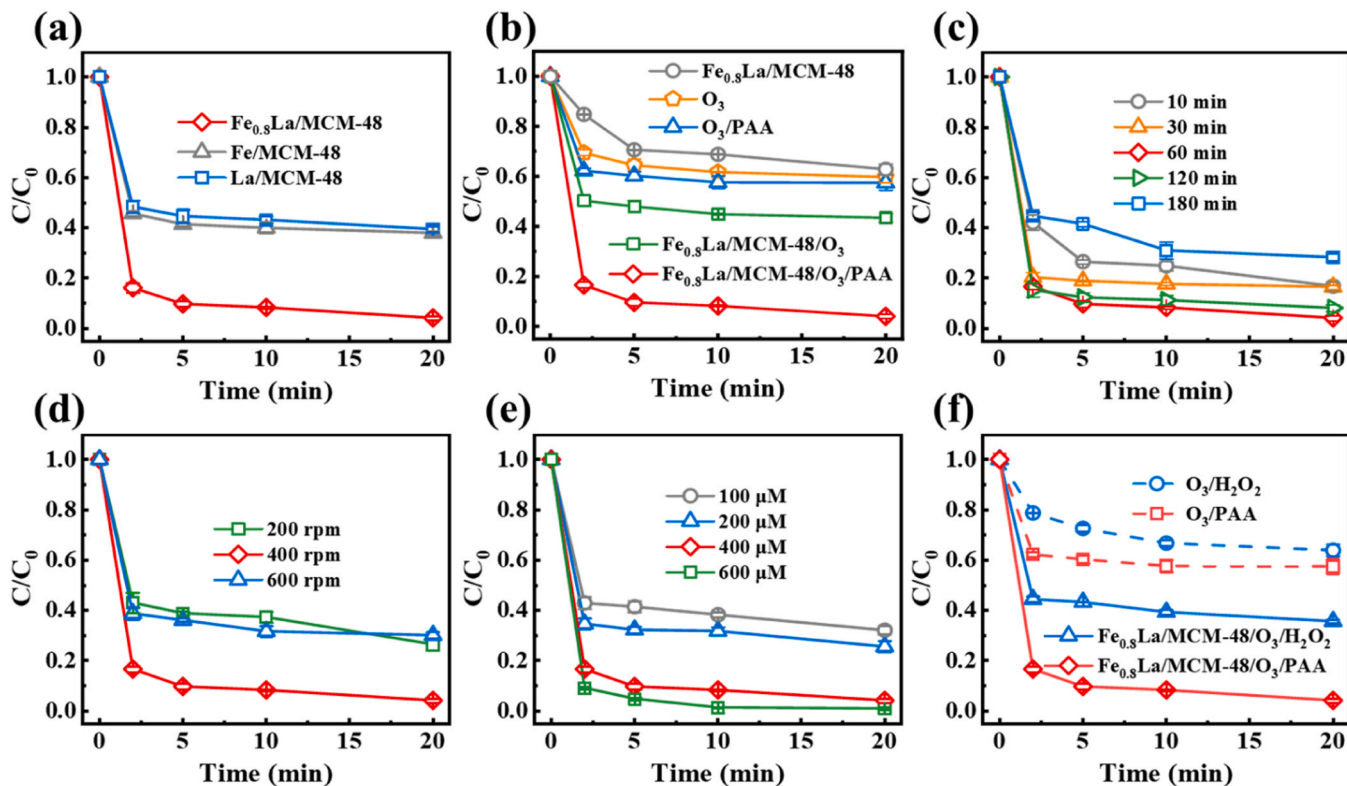


Fig. 3. TCH degradation in (a) monometal and bimetal catalysts and (b) different process; Effect of (c) milling time, (d) milling speed and (e) PAA dosages on the catalytic performance of Fe_{0.8}La/MCM-48 in the Fe_{0.8}La/MCM-48/O₃/PAA system; (f) Comparison of O₃/H₂O₂ and O₃/PAA process. Reaction conditions: [TCH] = 20 mg/L, [O₃] = 1 mg/L, [PAA] = 400 μM, [Catalyst] = 0.05 g/L.

shown in Figure S8, TCH degradation efficiency was enhanced from 81.2% to 96.0% with the increase of catalyst dosage from 0.025 g/L to 0.05 g/L. Nevertheless, further increasing catalyst dosage to 0.1 g/L would only lead to a slight improvement of TCH degradation efficiency. Therefore, 0.05 g/L is the optimum catalyst dosage. Figure S9 showed the catalytic activity and oxygen vacancies content of catalysts with different Fe/La molar ratios. The optimum Fe/La molar ratio was 0.8. Furthermore, the catalytic activities of catalysts with different Fe/La molar ratios were not positively correlated with the oxygen vacancies content, indicating that oxygen vacancies are not the only factor affecting the catalytic activity of the catalyst. As shown by the results of XPS and XAFS, La can also regulate the chemical environment of the Fe sites thereby affecting the catalytic activity. To further optimize $\text{Fe}_{0.8}\text{La}/\text{MCM-48}$, the effect of ball milling time and ball milling speeds was investigated in Fig. 3c-d. When the ball milling time increased from 10 to 60 min, the TCH degradation efficiency increased from 82.8% to 96.0%. This is attributed to the fact that the increase in ball milling time reduces the particle size of the catalyst and uniformly disperses the

metal to expose more active sites [47]. However, the degradation efficiency of TCH decreased with the extension of ball milling time. Figure S10 showed a significant decrease in the specific surface area of $\text{Fe}_{0.8}\text{La}/\text{MCM-48}$ due to prolonged ball milling time, suggesting that excessive energy input disrupts the ordered three-dimensional mesoporous structure of MCM-48. In addition, the optimum ball milling speed was 400 rpm. With the higher ball milling speeds, the ordering degree of catalyst decreases, leading to the poorer degradation of TCH. Therefore, it seemed that the effect of ball milling speed on catalyst structure was similar to that of ball milling time. The TCH degradation efficiency exhibited a positive dependence on the PAA dosage from 100 to 600 μM , which attributed to the ROS generation associated with PAA activation in Fig. 3e. Considering the chemical cost, 400 μM PAA was economically favorable as the optimal PAA dosage for the degradation of TCH.

The homolytic cleavage of the O–O bond could occur in PAA and H_2O_2 molecule. To further confirm the oxidation effect of H_2O_2 and the role of H_2O_2 as oxidants in the reaction was also evaluated. In

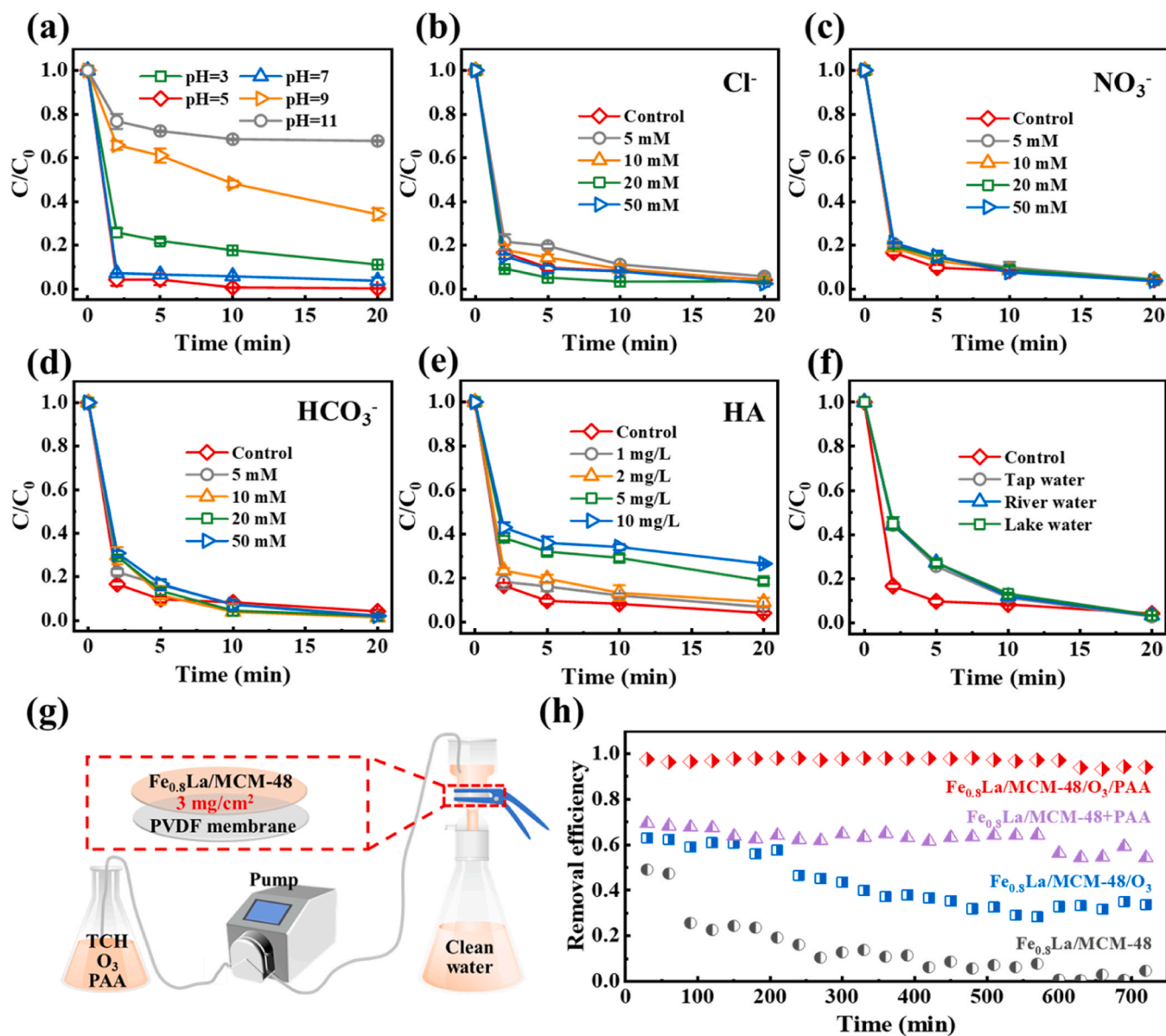


Fig. 4. Effect of (a) pH, (b) Cl^- , (c) NO_3^- , (d) HCO_3^- , (e) HA and (f) real water conditions on the degradation efficiency of TCH; (g) Schematic diagram of continuous flow-through device; (h) TCH removal efficiency in continuous flow system. Reaction conditions: $[\text{TCH}] = 20 \text{ mg/L}$, $[\text{O}_3] = 1 \text{ mg/L}$, $[\text{PAA}] = 400 \mu\text{M}$, $[\text{Catalyst}] = 0.05 \text{ g/L}$.

Figure S11, the degradation efficiency of TCH increased by only 7.8% in $\text{Fe}_{0.8}\text{La}/\text{MCM-48}/\text{O}_3/\text{H}_2\text{O}_2$ system when H_2O_2 concentration was increased from 100 to 400 μM . These results suggested that co-existing H_2O_2 did not contribute significantly to TCH degradation. Moreover, experiments were designed by comparing $\text{O}_3/\text{H}_2\text{O}_2$ and O_3/PAA processes on TCH degradation at the same doses in **Fig. 3f**. As expected, the results showed that O_3/PAA process outperformed the $\text{O}_3/\text{H}_2\text{O}_2$ process in TCH degradation regardless of the presence or absence of catalyst. It has been well documented that compared with H_2O_2 , PAA has the lower peroxy bond energy ($\text{PAA} = 38 \text{ kcal/mol}$; $\text{H}_2\text{O}_2 = 51 \text{ kcal/mol}$) and lowest unoccupied molecular orbital energy ($E_{\text{LUMO, PAA}} = -0.25 \text{ eV}$; $E_{\text{LUMO, H}_2\text{O}_2} = 0.57 \text{ eV}$), indicating that the formation of ROS in PAA activation may occur with lower energy demand [48]. Thus, more ROS were formed during the catalytic O_3/PAA process to promote TCH degradation. Remarkably, more than 90% degradation of TCH within 20 min was achieved in the first to third runs and the removal efficiency remained high at 85.2% after the fifth cycle, indicating the excellent stability of $\text{Fe}_{0.8}\text{La}/\text{MCM-48}$ during O_3/PAA activation (**Figure S12**).

Initial pH would affect the surface charge of materials, decomposition of oxidants and ionisation of pollutant molecules [49]. The effect of initial pH on TCH degradation was investigated in **Fig. 4a**. Obviously, the process efficiency showed hardly any dependence on pH in the range of 5.0–7.0, while an inhibition could be observed as the initial pH decreased from 5 to 3 (from 99.9% to 88.9%). This may be explained by electrostatic interactions between the catalyst ($\text{pH}_{\text{pzc}}=4.14$) (**Figure S13**) and the fully protonated TCH^+ cation and previous study illustrated that the TCH molecules exist as a zwitterion TCH^\pm at $3.30 < \text{pH} < 7.68$ [50]. Notably, the pH was increased from 5 to 7, TCH degradation was also inhibited due to the increased negative charge on the catalyst surface and the dissociation of pollutant molecules. Meanwhile, the degradation rate of TCH significantly reduced to 65.9% and 32.3% due to the strong electrostatic repulsion between $\text{Fe}_{0.8}\text{La}/\text{MCM-48}$, PAA^- and $\text{TCH}^-/\text{TCH}^{2-}$ under alkaline condition at pH 9 and 11. In this case, the anionic species of PAA (PAA^-) is dominant at alkaline conditions due to the pK_a value of PAA of 8.2 and the anionic $\text{TCH}^-/\text{TCH}^{2-}$ exists within the pH range of 7.68–9.70 and $\text{pH} > 9.70$, respectively [51].

Moreover, given that actual municipal wastewater treatment invariably contain the presence of coexisting compounds, the efficiency of TCH degradation in the presence of dissolved organic matter and inorganic anions was evaluated (**Fig. 4b–e**). Notably, the ionic constituents, including Cl^- , NO_3^- , HCO_3^- and low concentration of humic acid (HA), exhibited a minimal influence on TCH removal within the $\text{Fe}_{0.8}\text{La}/\text{MCM-48}/\text{O}_3/\text{PAA}$ system, which underscored the versatile effectiveness of the $\text{Fe}_{0.8}\text{La}/\text{MCM-48}/\text{O}_3/\text{PAA}$ system in the face of different coexisting ions. When the HA concentration increased to 5 mg/L and 10 mg/L, the degradation efficiency of TCH decreased to 81.5% and 73.5%, respectively. This may be attributed to the fact that HA competes with TCH for adsorption sites on the catalyst surface or acts as a ROS scavenger. In the course of proceeding oxidation experiments in actual water matrices (e.g., lake water, tap water and river water), which were harvested from the Beijing region in China (**Fig. 4f**). Nearly complete removal of TCH was still achieved within 20 min, demonstrating the robust stability of the $\text{Fe}_{0.8}\text{La}/\text{MCM-48}/\text{O}_3/\text{PAA}$ system regardless of different water matrices. $\text{Fe}_{0.8}\text{La}/\text{MCM-48}$, $\text{Fe}_{0.8}\text{La}/\text{MCM-48}/\text{O}_3$, $\text{Fe}_{0.8}\text{La}/\text{MCM-48}/\text{PAA}$ and $\text{Fe}_{0.8}\text{La}/\text{MCM-48}/\text{O}_3/\text{PAA}$ system were applied in a microreactor to examine its TCH removal efficiency (**Fig. 4h**). The physical device and the catalysts after the reaction were exhibited in **Figure S14**. A PVDF membrane (PFB) as the base was applied to fix the 3 mg/cm² samples at 52 mL/min average flow rate for continuous experiment. We observed that the TCH removal efficiency in the $\text{Fe}_{0.8}\text{La}/\text{MCM-48}/\text{O}_3/\text{PAA}$ system was maintained at 94% for more than 12 h, which was much higher than $\text{Fe}_{0.8}\text{La}/\text{MCM-48}/\text{O}_3$ (33.4%) and $\text{Fe}_{0.8}\text{La}/\text{MCM-48}/\text{PAA}$ processes (54.3%), demonstrating the high activity and stability of the system.

3.3. Identification of reactive oxygen species

1,10 phenanthroline was employed as a masking agent for Fe sites due to the formation of Fe-1,10 phenanthroline complex [52]. The addition of 10 mM 1,10 phenanthroline had no effect on the TCH degradation by the $\text{MCM-48}/\text{O}_3/\text{PAA}$ system and it demonstrated that 1,10 phenanthroline only played the role of a metal site masking agent in the $\text{Fe}_{0.8}\text{La}/\text{MCM-48}/\text{O}_3/\text{PAA}$ system. (**Figure S15a**). **Figure S15b** demonstrates that the degradation efficiency of TCH was reduced by 61.8% in the presence of 1,10 phenanthroline. Meanwhile, experiments were designed by adding 1,10 phenanthroline to the $\text{La}/\text{MCM-48}/\text{O}_3/\text{PAA}$ system to detect whether the La sites would be masked (**Figure S15c**). Remarkably, the degradation rate of TCH decreased by only 9.8% after 20 min in the presence of 1,10 phenanthroline and these results indicated that Fe sites played a key role in the TCH degradation.

In situ EPR technique was performed to identify the ROS using 5,5-dimethyl-1-pyrroline N-oxide (DMPO) and 2,2,6,6-tetramethyl-4-piperidinol (TEMP) as spin trapping agents. When DMPO was present, no EPR signals of $\cdot\text{OH}$, $\text{R-O}\cdot$ and $\text{O}_2^{\cdot-}$ were detected in O_3/PAA , $\text{Fe}_{0.8}\text{La}/\text{MCM-48}/\text{O}_3$ or $\text{Fe}_{0.8}\text{La}/\text{MCM-48}/\text{O}_3/\text{PAA}$ systems (**Figure S16**). These results demonstrated the absence of $\cdot\text{OH}$, $\text{R-O}\cdot$ and $\text{O}_2^{\cdot-}$ in $\text{Fe}_{0.8}\text{La}/\text{MCM-48}/\text{O}_3/\text{PAA}$ system. In contrast, the triplet $\text{TEMP-}^1\text{O}_2$ signals were detected in different reaction systems, suggesting the generation of $^1\text{O}_2$ (**Fig. 5a**). The weaker $\text{TEMP-}^1\text{O}_2$ signals appeared in the presence of PAA alone, which attributed to the low self-decomposition of PAA [53]. The addition of $\text{Fe}_{0.8}\text{La}/\text{MCM-48}$ promoted decomposition of PAA to produce $^1\text{O}_2$. Additionally, the weak $^1\text{O}_2$ signal also appears in the $\text{Fe}_{0.8}\text{La}/\text{MCM-48}/\text{O}_3$ system. $^1\text{O}_2$ in catalytic ozonation can be produced by three pathways: disproportionation of $\text{O}_2^{\cdot-}/\text{HO}_2^{\cdot}$ (Eq. 1), the reaction of $\text{O}_2^{\cdot-}$ with $\cdot\text{OH}$ (Eq. 2), and the transformation of surface-adsorbed peroxides or free peroxides from O_3 decomposition (Eq. 3) [54]. However, the pathway for the disproportionation of $\text{O}_2^{\cdot-}$ and the reaction of $\text{O}_2^{\cdot-}$ and $\cdot\text{OH}$ to produce $^1\text{O}_2$ is ruled out due to the absence of $\text{O}_2^{\cdot-}$ and $\cdot\text{OH}$ in the $\text{Fe}_{0.8}\text{La}/\text{MCM-48}/\text{O}_3$ system. This suggested that $^1\text{O}_2$ may originate from surface-adsorbed or free peroxides produced by $\text{Fe}_{0.8}\text{La}/\text{MCM-48}$ -catalyzed ozone decomposition.



When O_3 and PAA were simultaneously added to the solution, the intensity of $\text{TEMP-}^1\text{O}_2$ signal was stronger than PAA alone. This has been reported that synergistic ozonation, such as $\text{O}_3/\text{H}_2\text{O}_2$, O_3/PMS or O_3/SPC , showed considerably higher ROS yields [10,55]. It demonstrated that the synergism of O_3 and PAA promoted the generation of $^1\text{O}_2$ and it was the intensity of $\text{TEMP-}^1\text{O}_2$ signal was significantly enhanced by the addition of $\text{Fe}_{0.8}\text{La}/\text{MCM-48}$, indicating that $\text{Fe}_{0.8}\text{La}/\text{MCM-48}$ can effectively catalyze O_3/PAA reaction to generate more $^1\text{O}_2$. Meanwhile, quenching experiments were conducted by using different quenching agents (**Fig. 5b**). MeOH usually serve as quenchers for both $\text{R-O}\cdot$ and $\cdot\text{OH}$, while TBA is used as a selective radical $\cdot\text{OH}$ quencher [56]. And CF was used to quench $\text{O}_2^{\cdot-}$. Apparently, the presence of these quenchers had much less limited suppression effect on TCH degradation, which was consistent with the results of EPR experiments. Comparatively, the degradation efficiency of TCH decreased by 24.4% in the presence of FFA as the quencher of $^1\text{O}_2$ and this also indicated that $^1\text{O}_2$ might play an important role in TCH degradation. To further verify the role of $^1\text{O}_2$, the degradation of TCH in $\text{Fe}_{0.8}\text{La}/\text{MCM-48}/\text{O}_3/\text{PAA}$ in D_2O solution was performed and we could observed that this degradation efficiency was slightly higher than that in H_2O , which could be ascribed to the longer lifetime of $^1\text{O}_2$ in D_2O (**Fig. 5c**) [57]. To understand the origin of $^1\text{O}_2$, the saturated dissolved oxygen (DO) experiment was carried out due to that DO could be activated to generate $\text{O}_2^{\cdot-}$ and

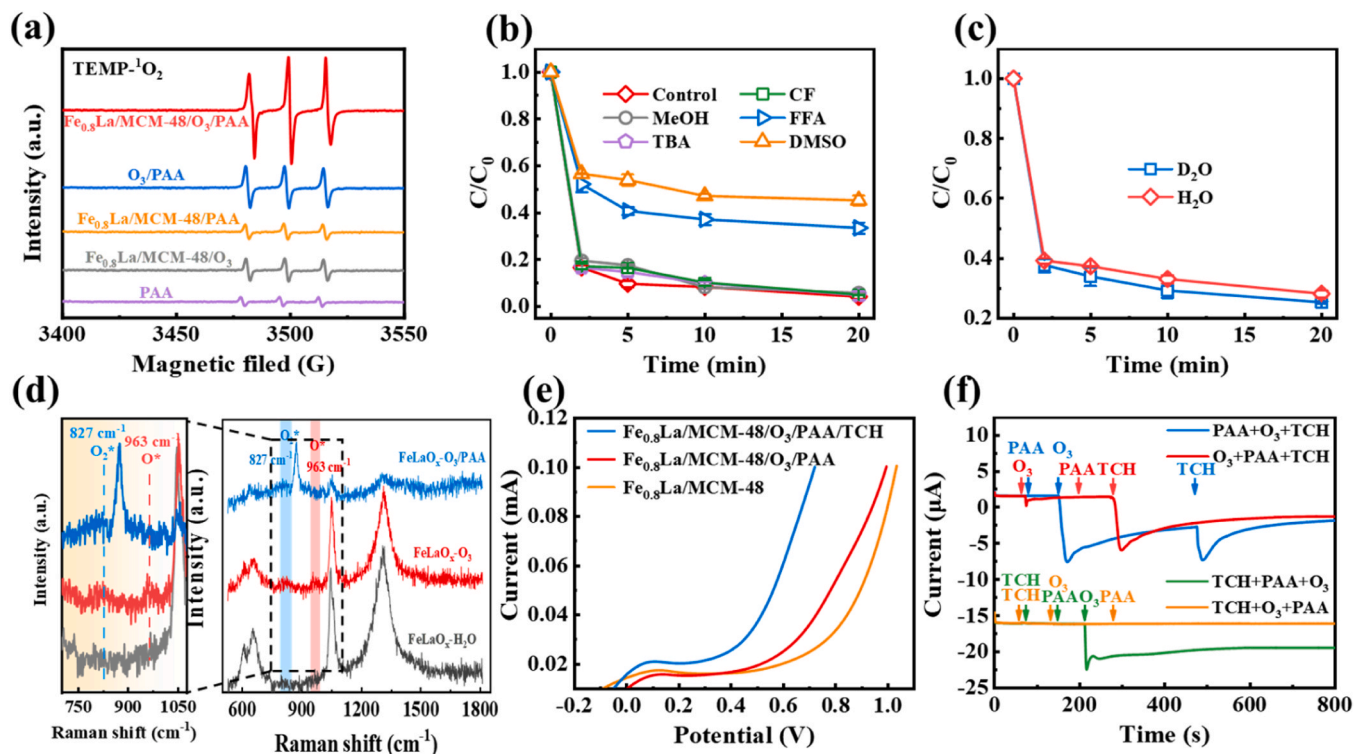


Fig. 5. (a) EPR spectrum of TEMP-¹O₂; (b) Effect of different capture agents on the degradation of TCH; (c) 25 mg/L TCH degradation in Fe_{0.8}La/MCM-48/O₃/PAA system in H₂O/D₂O matrix; (d) In situ Raman spectra in different systems; (e) LSV tests in the presence of O₃/PAA or TCH; (f) Current responses after the sequential injection of O₃, PAA and TCH. Reaction conditions: [TCH] = 20 mg/L, [O₃] = 1 mg/L, [PAA] = 400 μM, [Catalyst] = 0.05 g/L, [quenchers] = 100 mM.

recombination of O₂^{•−} could be converted to generate ¹O₂ [58]. Notably, the degradation efficiency of TCH was not enhanced in the saturated DO environment indicated that ¹O₂ came from catalytic O₃/PAA reaction instead of DO and O₂^{•−} (Figure S17). In the meantime, lower PMSO consumption and PMSO₂ conversion rates suggested that high-valent metal-oxygen species are not the main ROS (Figure S18) [59]. Additionally, DMSO was used to assess the role of surface-adsorbed ROS [60]. DMSO can be used to quench *O_{ad}, surface radicals and high-valent metal oxygen species [61–63]. However, the absence of free radicals and limited contribution of high-valent metal species suggested that DMSO was mainly used to quench *O_{ad}. TCH removal was significantly impeded when DMSO was added to the solution, indicating that surface-adsorbed ROS also played an important role in TCH degradation (Fig. 5b). However, the above experiments demonstrated that surface-adsorbed ROS were not surface-adsorbed radical species owing to the absence of *OH, R–O* and O₂^{•−}. And the addition of DMSO had an inhibitory effect on TCH degradation in the Fe_{0.8}La/MCM-48/O₃ system, but no obvious effect on TCH degradation in the Fe_{0.8}La/MCM-48/PAA system (Figure S19). This suggested that the surface-adsorbed ROS originates from the reaction of Fe_{0.8}La/MCM-48 and O₃. As it is widely recognized, the decomposition of ozone on the catalyst surface was easy to result in the formation of surface *O_{ad} [61]. Thus, *O_{ad} might be an important ROS for TCH degradation in Fe_{0.8}La/MCM-48/O₃/PAA system. To prove this point, in situ Raman spectroscopy was applied to explore the interface reaction in the Fe_{0.8}La/MCM-48/O₃/PAA system (Fig. 5c). The simultaneous appearance of new Raman peak at 827 cm⁻¹ and 963 cm⁻¹ on the surface of FeLaO_x of the MCM-48 could be assigned to the stretching vibration of surface adsorbed peroxide (O₂^{••}) and *O_{ad} after adding O₃. However, with the addition of PAA, the peak belonging to *O_{ad} disappeared, indicating that *O_{ad} generated on the surface of catalysts, which can react with PAA to generate ¹O₂. 100 mM DMSO was added to the Fe_{0.8}La/MCM-48/O₃/PAA reaction system to quench the surface *O_{ad} in order to study the effect of surface *O_{ad} on ¹O₂ (Figure S20). The results showed that the addition of DMSO led to

the weakening of TEMP-¹O₂ signal, indicating that the surface *O_{ad} promoted the production of ¹O₂. To quantify the contribution of ¹O₂ in TCH degradation, we calculated the contribution of ¹O₂ based on the reaction kinetic constants in the quenching experiments and Figure S21 showed two stages of TCH degradation, the fast stage within 0–2 min and the slow stage within 2–20 min [64]. According to the kinetic constants, the contribution of ¹O₂ and *O_{ad} in the fast stage were 63.8% and 36.2%. In the slow stage, the contributions of ¹O₂ and *O_{ad} were 70.1% and 29.9%. This suggested that ¹O₂ is the dominant active species in Fe_{0.8}La/MCM-48/O₃/PAA system.

To ascertain the involvement of electron transfer in the Fe_{0.8}La/MCM-48/O₃/PAA system, electrochemical measurements were performed to explore the unique non-radical species process. In Fig. 5e, the current increased in the presence of O₃, PAA and TCH according to the results of linear sweep voltammetry (LSV) curve, certifying the occurrence of fast electron transfer between Fe_{0.8}La/MCM-48, O₃, PAA and TCH. The chronoamperometry test in Fig. 5f showed that no current response was observed once the injection of PAA. Noticeable current jump appeared upon the addition of O₃, which is attributed to the electron transfer resulting from the reaction of Fe_{0.8}La/MCM-48 and O₃ to form *O_{ad} [65]. The subsequent addition of TCH caused significant current jumps. In contrast, adding TCH at first did not cause change in the current. These results confirmed that TCH was not directly reduced by getting electron at the cathode. It was noteworthy that the prior addition of PAA caused significant current changes upon O₃ addition, which could be explained by the contribution of PAA to the electron transfer between catalysts and O₃.

3.4. Possible catalytic mechanism

The XPS spectra of Fe_{0.8}La/MCM-48 before and after TCH degradation reaction were displayed in Figure S22. In the XPS spectra of Fe 2p after reaction, the Fe 2p_{1/2} peak at 724.2 eV and the Fe 2p_{3/2} peak at 711.0 eV were attributed to Fe(II), and the Fe 2p_{1/2} peak at 727.4 eV and

the Fe 2p_{3/2} peak at 713.2 eV were assigned to Fe(III) [37]. The XPS spectra of Fe 2p for Fe_{0.8}La/MCM-48 before and after reaction located at similar binding energy. However, the relative proportion of Fe(II) decreased slightly from 58.8% to 56.6% and the relative proportion of Fe(III) increased from 41.2% to 43.4%. This indicated that Fe(II) supplied electrons to ozone and was oxidized to Fe(III) [66]. There was no significant change in XPS spectra of La 3d before and after the reaction, which suggested that La does not take part in the degradation of TCH.

We then conducted DFT calculations to elucidate the electronic structure of Fe_{0.8}La/MCM48 and the in-depth mechanism of O₃ and PAA on Fe_{0.8}La/MCM-48 at the molecular level. Firstly, the La-doped configurations were determined from the XAFS results (Figure S23a). The optimal location of the oxygen vacancy was determined by the formation energy of the oxygen vacancy at different locations (Figure S23). LaOv-1 has the lowest formation energy, which indicates that oxygen vacancy at this location are easier to form and more stable (Table S5). Thus, the final configuration was determined to be LaOv-Fe₂O₃ with the lowest oxygen vacancy formation. Fe₂O₃, La-Fe₂O₃, Ov-Fe₂O₃ and LaOv-Fe₂O₃ configurations were constructed for exploring the electronic structure (Figure S24). The oxygen vacancy formation energies of Ov-Fe₂O₃ and LaOv-Fe₂O₃ were calculated to be +7.49 and +1.44 eV (Fig. 6a). The lower oxygen vacancy formation energy of LaOv-Fe₂O₃ indicated that La doping could promote the generation of oxygen

vacancies and thus changed the electronic structure of the catalyst. The partial density of states (PDOS) results showed that La doping and oxygen vacancies were contributed to optimize the bonding orbital distribution near the Fermi energy level (Fig. 6b). It was noted that the density of states of LaOv-Fe₂O₃ at Fermi energy level was more intensive and closer to Fermi energy level compared to La-Fe₂O₃ and Ov-Fe₂O₃, indicating a more favorable chemical interaction with O₃ or PAA. In addition, the *d*-band center of Fe in LaOv-Fe₂O₃ (−1.50 eV) shifts positively compared to Fe₂O₃ (−2.49 eV), La-Fe₂O₃ (−2.02 eV) and Ov-Fe₂O₃ (−1.70 eV), much closer to the Fermi energy level. The upward shift of *d*-band center was conducive to enhance the adsorption of O₃ or PAA [67]. Based on these findings, Fe–O–La and oxygen vacancies regulated the electronic structure of catalysts, enhancing the adsorption of O₃ or PAA. Additionally, ELF (Electron Localization Function) results show that La doping might cause distortion on the lattice surface of Fe₂O₃ and change the surface electronic structure of the catalyst, which led to the more electrons gather around oxygen vacancy and formed an electron-rich center (Fig. 6c). Then the nearby Fe atoms would be as electron-poor center as the transfer and loss of electrons, which is consistent with the XAFS results. The calculated adsorption energies of O₃ and PAA onto well-defined active sites configurations of Fe_{0.8}La/MCM-48 were −2.62 and −0.73 eV, respectively, indicating that the former showed a stronger chemisorption capacity than the latter (Fig. 6d). And it is noteworthy

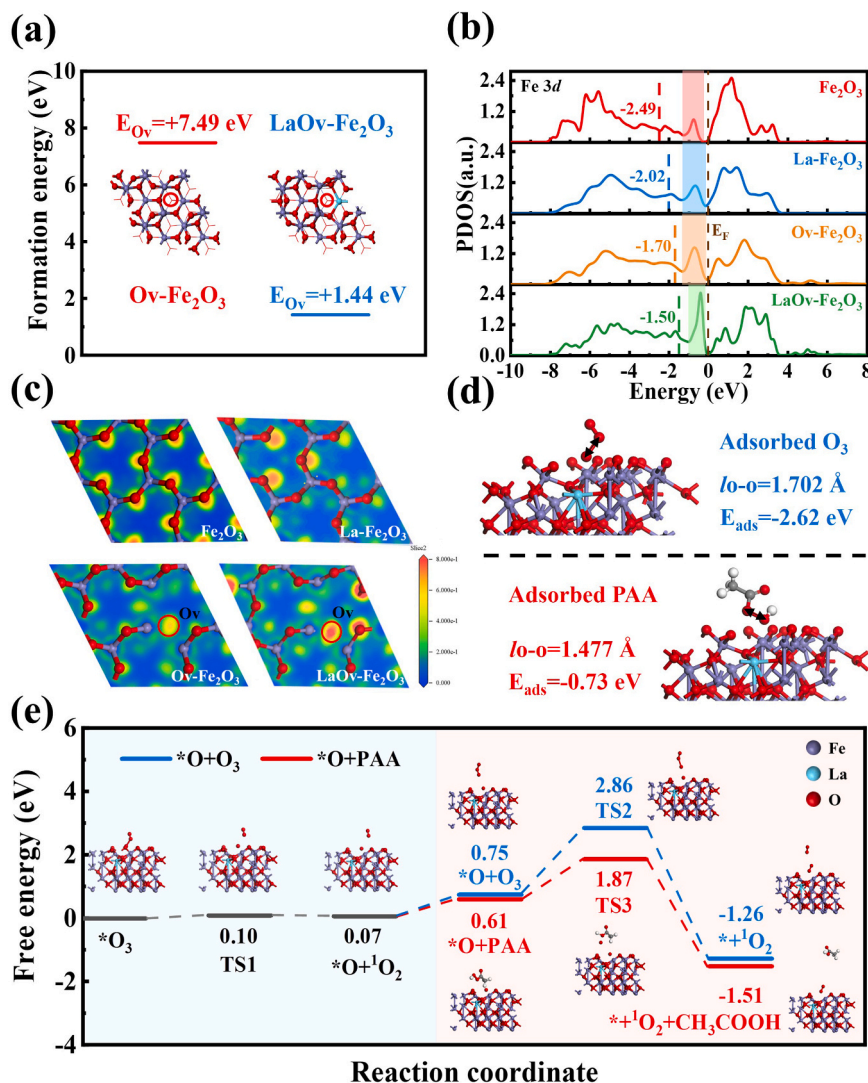


Fig. 6. (a) PDOS of Fe 3d; (b) Oxygen vacancies formation energy; (c) ELF maps; (d) Adsorption of O₃ and PAA on Fe_{0.8}La/MCM-48; (e) Free energy diagram of the reaction pathway.

that the adsorption energies of O_3 and PAA adsorption on samples were both negative ($\Delta E_{ads} < 0$), confirming the energetically favorable nature of these processes. During O_3 and PAA activation on catalysts, O_3 molecules might well firstly adsorbed onto the surface to form catalyst- O_3 complexes and then activated through PAA oxidation over electron-poor areas. Based on this speculation, the Mulliken population analysis was performed and the result showed that the electron transfer between $Fe_{0.8}La/MCM-48$ and adsorbed O_3 was $0.20 e^-$, which was higher than between $Fe_{0.8}La/MCM-48$ and adsorbed PAA ($0.10 e^-$). Namely, the lower adsorption energy and higher electron transfer between O_3 and $Fe_{0.8}La/MCM-48$ suggested that $Fe_{0.8}La/MCM-48$ reacts more strongly with O_3 [68]. For the adsorption structure of O_3 on $Fe_{0.8}La/MCM-48$, the O–O bond length (l_{O-O}) of O_3 was measured to be 1.702 \AA , which was significantly increased compared with that of initial O_3 (1.274 \AA), indicating that the O–O bond was easily broken to generate ROS (Figure S25) [68]. To differentiate the dissociation and desorption processes of between surface $*O_{ad}$ and reactive species on active site configuration of $Fe_{0.8}La/MCM-48$, optimized potential free energy diagrams during reaction were computed assuming the O_3 and PAA activation process (Fig. 6e). The simulation results demonstrated that when the O_3 was adsorbed on the catalyst surface, the O–O bond on the surface was stretched and broken, resulting in the formation of bonded $*O_{ad}$ and free O_2 , along with overcoming an energy barrier of 0.10 eV . Combined with previous studies and EPR experiments, the resulting free O_2 was estimated to be 1O_2 . Meanwhile, the surface $*O_{ad}$ could further combine with O_3 to form 1O_2 . The intermediate transition state of TS2 and TS3 generation has the largest energy barrier, which was regarded as the rate-determining step. The surface $*O_{ad}$ would combine with PAA through intermediate states TS3 to generate 1O_2 and CH_3COOH , which

required overcoming a lower reaction energy barrier than the binding of surface $*O_{ad}$ to O_3 . Therefore, it could be concluded the bonding between the added PAA and surface $*O_{ad}$ promoted the generation of 1O_2 and thus improved the degradation efficiency of TCH.

3.5. Identification of intermediates and possible degradation pathways

To figure out the degradation pathways of TCH in the $Fe_{0.8}La/MCM-48/O_3/PAA$ system, HPLC–MS was employed to test the produced intermediates. The corresponding mass spectral data of these intermediates were shown in Figure S26 and molecular structures were listed in Table S4. Firstly, TCH was dissociated as tetracycline. Based on this, the possible degradation pathways of tetracycline were exhibited in Fig. 7b. For pathway I, tetracycline ($m/z = 445.1611$) molecule underwent hydroxylation and the oxidation of –OH group into carbonyl group to produce P1 ($m/z = 461.1563$) [69]. Then P1 was dehydroxylated to form P4 ($m/z = 425.2151$) [70]. And the generation of P3 ($m/z = 477.1510$) was attributed to the oxidation of double bond on P1. The –N(CH_3)₂ group in P3 was attacked to generate P5 ($m/z = 448.2924$) [71]. Furthermore, P3 can be converted to P6 ($m/z = 403.2338$) by amine group demethylation and loss of methyl and adjacent hydroxyl groups on the benzene ring [72]. Additionally, P7 ($m/z = 310.9542$) was formed from P3 through ring opening, dealkylation, dehydration, decarbonylation and dihydroxylation [73]. In pathway II, P2 ($m/z = 301.1416$) was generated through the process of dehydration and ring opening. Then, P8 ($m/z = 279.1594$) was produced by opening of double bond and decarboxylation. In addition, P2 were transformed separately into P9 ($m/z = 269.9281$) and P10 ($m/z = 284.0875$) through dehydration and demethylation [74]. Subsequently, P10 decomposed

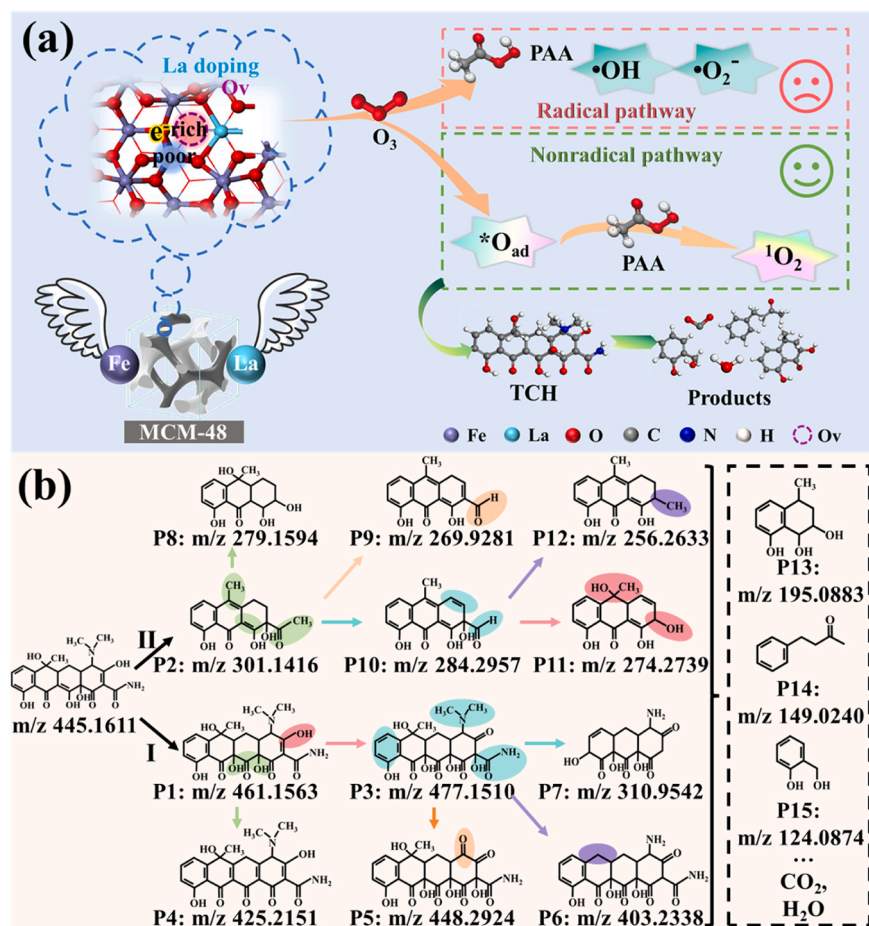


Fig. 7. (a) Possible reaction mechanism of $Fe_{0.8}La/MCM-48/O_3/PAA$ system and (b) degradation pathways of TCH in $Fe_{0.8}La/MCM-48/O_3/PAA$ system.

into P11 ($m/z = 274.2739$) and P12 ($m/z = 256.2633$). Finally, some macromolecular further decomposed into small molecules, and these small molecules were further mineralized into CO_2 and H_2O . ECOSAR was applied to predict the acute and chronic toxicity of TCH and its transformation products and details were listed in Table S7. As shown in Figure S27, most of the transformation products exhibited lower ecotoxicity than TCH. In the acute toxicity analysis, most of the transformed products were not harmful to aquatic organisms. P2 and P10 were harmful to aquatic organisms, while P7 were harmful to daphnid and green algae. Chronic toxicity analysis found most of the transformation products to be harmful to aquatic organisms, but were less toxic than TCH. The above analysis suggested that the $\text{Fe}_{0.8}\text{La}/\text{MCM-48}$ catalyzed O_3/PAA process can reduce the ecological risk of TCH.

4. Conclusion

In this work, the involvement of $^1\text{O}_2$ -dominated non-free radical pathway in O_3/PAA activation by $\text{Fe}_{0.8}\text{La}/\text{MCM-48}$ has been observed and confirmed. The $\text{Fe}_{0.8}\text{La}/\text{MCM-48}$ suspension showed a higher degradation efficiency of TCH during the heterogenous PAA and O_3 system under the synergistic action of Fe and La. Additionally, TCH removal efficiency in the $\text{Fe}_{0.8}\text{La}/\text{MCM-48}$ membrane microreactor in O_3/PAA system was maintained at 94% for more than 12 h. Specifically, the role of oxygen vacancies in bridging the electron regulation and reaction route onto the interface has been elucidated. The surface $^*\text{O}_{\text{ad}}$ would combine with PAA to generate $^1\text{O}_2$ and CH_3COOH according to the results of DFT calculation, which required overcoming a lower reaction energy barrier than the binding of surface $^*\text{O}_{\text{ad}}$ to O_3 . Meanwhile, the upward shift of d -band center along with the lower adsorption energy and higher electron transfer were conducive to enhance the interaction of O_3 or PAA and $\text{Fe}_{0.8}\text{La}/\text{MCM-48}$ reacts more strongly with O_3 . TCH molecule would undergo hydroxylation, dehydration, ring opening and the oxidation of $-\text{OH}$ group into carbonyl group process. The findings of this study reveal the structure-activity relationship of $\text{Fe}_{0.8}\text{La}/\text{MCM-48}$ and $^1\text{O}_2$ generation in the novel heterogeneous O_3/PAA process for decomposing recalcitrant organic contaminants in wastewater.

CRediT authorship contribution statement

Tingting Zhang: Writing – review & editing, Supervision, Funding acquisition. **Shangyi Li:** Writing – review & editing, Supervision, Funding acquisition. **Yixiao Zou:** Methodology. **Yuhui Wang:** Methodology, Investigation. **Fengling Pan:** Writing – original draft, Methodology, Investigation, Data curation, Conceptualization. **Shuhan Fu:** Software, Methodology, Investigation.

Declaration of Competing Interest

The authors declare that they have no known competing financial interests or personal relationships that could have appeared to influence the work reported in this paper.

Data availability

Data will be made available on request.

Acknowledgements

This work was supported by the National Natural Science Foundation of China (No. 22206101), (No. 42277038) and Fundamental Research Funds for the Central Universities (buctrc202232).

Appendix A. Supporting information

Supplementary data associated with this article can be found in the online version at doi:10.1016/j.apcatb.2024.124185.

References

- [1] Y. Mao, H. Dong, S. Liu, L. Zhang, Z. Qiang, Accelerated oxidation of iopamidol by ozone/peroxymonosulfate (O_3/PMS) process: kinetics, mechanism, and simultaneous reduction of iodinated disinfection by-product formation potential, *Water Res.* 173 (2020) 115615, <https://doi.org/10.1016/j.watres.2020.115615>.
- [2] S. Guerra-Rodríguez, M.J. Abeledo-Lameiro, M.I. Polo-López, P. Plaza-Bolaños, A. Agüera, E. Rodríguez, J. Rodríguez-Chueca, Pilot-scale sulfate radical-based advanced oxidation for wastewater reuse: Simultaneous disinfection, removal of contaminants of emerging concern, and antibiotic resistance genes, *Chem. Eng. J.* 477 (2023) 146916, <https://doi.org/10.1016/j.cej.2023.146916>.
- [3] J. Gu, Y. Yang, Y. Song, J. Jiang, Theoretical insight into the initial reaction of ozone with peroxide: single electron transfer or adduct formation, *Chem. Eng. J.* 429 (2022) 132308, <https://doi.org/10.1016/j.cej.2021.132308>.
- [4] W. Qin, Z. Lin, H. Dong, X. Yuan, Z. Qiang, S. Liu, D. Xia, Kinetic and mechanistic insights into the abatement of clofibric acid by integrated UV/ozone/peroxydisulfate process: a modeling and theoretical study, *Water Res.* 186 (2020) 116336, <https://doi.org/10.1016/j.watres.2020.116336>.
- [5] S. Li, J. Huang, X. Li, L. Li, The relation of interface electron transfer and PMS activation by the H-bonding interaction between composite metal and MCM-48 during sulfamethazine ozonation, *Chem. Eng. J.* 398 (2020) 125529, <https://doi.org/10.1016/j.cej.2020.125529>.
- [6] X. Yin, J. Zhang, S. Chen, W. Li, H. Zhu, K. Wei, Y. Zhang, H. Chen, W. Han, Electric field-enhanced heterogeneous catalytic ozonation (EHCO) process for sulfadiazine removal: the role of cathodic reduction, *Chemosphere* 351 (2024) 141226, <https://doi.org/10.1016/j.chemosphere.2024.141226>.
- [7] L. Wu, Z. Sun, Y. Zhen, S. Zhu, C. Yang, J. Lu, Y. Tian, D. Zhong, J. Ma, Oxygen vacancy-induced nonradical degradation of organics: critical trigger of oxygen (O_2) in the Fe-Co LDH/peroxymonosulfate system, *Environ. Sci. Technol.* 55 (2021) 15400–15411, <https://doi.org/10.1021/acs.est.1c04600>.
- [8] Z. Guo, Y. Xie, J. Xiao, Z.-J. Zhao, Y. Wang, Z. Xu, Y. Zhang, L. Yin, H. Cao, J. Gong, Single-atom Mn-N₄ site-catalyzed peroxide reaction for the efficient production of hydroxyl radicals in an acidic solution, *J. Am. Chem. Soc.* 141 (2019) 12005–12010, <https://doi.org/10.1021/jacs.9b04569>.
- [9] M. Kohantorabi, G. Moussavi, P. Oulego, S. Giannakis, Heterogeneous catalytic ozonation and peroxide-mediated removal of Acetaminophen using natural and modified hematite-rich soil, as efficient and environmentally friendly catalysts, *Appl. Catal. B Environ.* 301 (2022) 120786, <https://doi.org/10.1016/j.apcatb.2021.120786>.
- [10] Q.-Y. Wu, The promotions on radical formation and micropollutant degradation by the synergies between ozone and chemical reagents (synergistic ozonation): a review, *J. Hazard. Mater.* 418 (2021) 126327, <https://doi.org/10.1016/j.jhazmat.2021.126327>.
- [11] J. Liang, X. Duan, X. Xu, K. Chen, Y. Zhang, L. Zhao, H. Qiu, S. Wang, X. Cao, Persulfate oxidation of sulfamethoxazole by magnetic iron-char composites via nonradical pathways: Fe(IV) versus surface-mediated electron transfer, *Environ. Sci. Technol.* 55 (2021) 10077–10086, <https://doi.org/10.1021/acs.est.1c01618>.
- [12] A. Jawad, K. Zhan, H. Wang, A. Shahzad, Z. Zeng, J. Wang, X. Zhou, H. Ullah, Z. Chen, Z. Chen, Tuning of persulfate activation from a free radical to a nonradical pathway through the incorporation of non-redox magnesium oxide, *Environ. Sci. Technol.* 54 (2020) 2476–2488, <https://doi.org/10.1021/acs.est.9b04696>.
- [13] X. Duan, H. Sun, Z. Shao, S. Wang, Nonradical reactions in environmental remediation processes: uncertainty and challenges, *Appl. Catal. B Environ.* 224 (2018) 973–982, <https://doi.org/10.1016/j.apcatb.2017.11.051>.
- [14] Z. Fang, J. Qi, W. Chen, L. Zhang, J. Wang, C. Tian, Q. Dai, W. Liu, L. Wang, Defect engineering-mediated Co_9S_8 with unexpected catalytic selectivity for heterogeneous Fenton-like reaction: unveiling the generation route of $^1\text{O}_2$ in VS active site, *Appl. Catal. B Environ.* 338 (2023) 123084, <https://doi.org/10.1016/j.apcatb.2023.123084>.
- [15] Z. Weng, Y. Lin, B. Han, X. Zhang, Q. Guo, Y. Luo, X. Ou, Y. Zhou, J. Jiang, Donor-acceptor engineered g-C₃N₄ enabling peroxymonosulfate photocatalytic conversion to $^1\text{O}_2$ with nearly 100% selectivity, *J. Hazard. Mater.* 448 (2023) 130869, <https://doi.org/10.1016/j.jhazmat.2023.130869>.
- [16] C. Sui, Z. Nie, H. Liu, G. Boczkaj, W. Liu, L. Kong, J. Zhan, Singlet oxygen-dominated peroxymonosulfate activation by layered crednerite for organic pollutants degradation in high salinity wastewater, *J. Environ. Sci.* 135 (2024) 86–96, <https://doi.org/10.1016/j.jes.2023.01.010>.
- [17] Z. Xie, C. He, Y. He, S. Yang, S. Yu, Z. Xiong, Y. Du, Y. Liu, Z. Pan, G. Yao, B. Lai, Peracetic acid activation via the synergic effect of Co and Fe in CoFe-LDH for efficient degradation of pharmaceuticals in hospital wastewater, *Water Res.* 232 (2023) 119666, <https://doi.org/10.1016/j.watres.2023.119666>.
- [18] R. Ning, Y. Dong, S. Yang, S. Yang, P. Zhou, Z. Xiong, Z. Pan, C. He, B. Lai, Fe-N doped biochar derived from biomass waste triggers peracetic acid activation for efficient water decontamination, *J. Hazard. Mater.* 470 (2024) 134139, <https://doi.org/10.1016/j.jhazmat.2024.134139>.
- [19] G. Fan, L. Yao, Y. Wang, X. Peng, J. Xu, S. Pang, K. Xu, B. Du, J. Chen, Z. Hong, The dual pathway mechanisms of peroxyacetic acid activation by CoMn_2O_4 spinel for efficient levofloxacin degradation, *J. Environ. Chem. Eng.* 11 (2023) 109774, <https://doi.org/10.1016/j.jece.2023.109774>.
- [20] S. Li, Y. Yang, H. Zheng, Y. Zheng, C.-S. He, B. Lai, J. Ma, J. Nan, Introduction of oxygen vacancy to manganese ferrite by Co substitution for enhanced peracetic acid activation and $^1\text{O}_2$ dominated tetracycline hydrochloride degradation under microwave irradiation, *Water Res.* 225 (2022) 119176, <https://doi.org/10.1016/j.watres.2022.119176>.
- [21] S. Chen, T. Ren, K. Lu, C. Ouyang, X. Huang, X. Zhang, MnNx-carbon-silica-framework for highly efficient heterogeneous catalytic ozonation of electron-rich

- organics through nonradical pathway, *Chem. Eng. J.* 466 (2023) 143110, <https://doi.org/10.1016/j.cej.2023.143110>.
- [22] Q. Qin, T. Liu, J. Zhang, R. Wei, S. You, Y. Xu, Facile synthesis of oxygen vacancies enriched α -Fe₂O₃ for peroxymonosulfate activation: a non-radical process for sulfamethoxazole degradation, *J. Hazard. Mater.* 419 (2021) 126447, <https://doi.org/10.1016/j.jhazmat.2021.126447>.
- [23] H. Zhong, X. Ji, C. Yang, C. Tang, X. Hu, J. Cai, Q. Yin, J. Wang, X. Hu, X. Tan, M. Zhu, Z-scheme heterojunction α -Fe₂O₃/tubular g-C₃N₄ with C defects for photocatalytic degradation of microcystin-LR in water: generation and effect of critical species ¹O₂, *ACS Catal.* 14 (2024) 6272–6291, <https://doi.org/10.1021/acscatal.4c00121>.
- [24] S. Guo, H. Wang, W. Yang, H. Fida, L. You, K. Zhou, Scalable synthesis of Ca-doped α -Fe₂O₃ with abundant oxygen vacancies for enhanced degradation of organic pollutants through peroxymonosulfate activation, *Appl. Catal. B Environ.* 262 (2020) 118250, <https://doi.org/10.1016/j.apcatb.2019.118250>.
- [25] P. Yang, Z. Cao, Y. Long, D. Liu, W. Huang, S. Zhan, M. Li, Regulating the local electronic structure of copper single atoms with unsaturated B₂O₃-coordination for selective ¹O₂ generation, *ACS Catal.* 13 (2023) 12414–12424, <https://doi.org/10.1021/acscatal.3c03303>.
- [26] Y. Wang, Y. Sun, M. Gao, C. Zhou, Y. Xin, G. Zhang, P. Xu, D. Ma, Indium-doped β -MnO₂ catalyst for activation of peroxymonosulfate to generate singlet oxygen with complete selectivity, *J. Clean. Prod.* 380 (2022) 134953, <https://doi.org/10.1016/j.jclepro.2022.134953>.
- [27] H. Zhang, X. Zheng, T. Xu, P. Zhang, Atomically dispersed Y or La on birnessite-type MnO₂ for the catalytic decomposition of low-concentration toluene at room temperature, *ACS Appl. Mater. Interfaces* 13 (2021) 17532–17542, <https://doi.org/10.1021/acsami.1c01433>.
- [28] X. Zhao, F. Yin, X. He, B. Chen, G. Li, Enhancing hydrogen evolution reaction activity on cobalt oxide in alkaline electrolyte by doping inactive rare-earth metal, *Electrochim. Acta* 363 (2020) 137230, <https://doi.org/10.1016/j.electacta.2020.137230>.
- [29] S. Li, J. Wang, Y. Ye, Y. Tang, X. Li, F. Gu, L. Li, Composite Si-O-metal network catalysts with uneven electron distribution: enhanced activity and electron transfer for catalytic ozonation of carbamazepine, *Appl. Catal. B Environ.* 263 (2020) 118311, <https://doi.org/10.1016/j.apcatb.2019.118311>.
- [30] S. Yao, R. Zheng, R. Li, Y. Chen, X. Zhou, X. Ning, L. Zhan, J. Luo, LaCoO₃ acts as a high-efficiency co-catalyst for enhancing visible-light-driven tetracycline degradation of BiOI, *J. Am. Ceram. Soc.* 103 (2020) 1709–1721, <https://doi.org/10.1111/jace.16839>.
- [31] J. Hou, C. Wang, D. Mao, Y. Luo, The occurrence and fate of tetracyclines in two pharmaceutical wastewater treatment plants of Northern China, *Environ. Sci. Pollut. Res. Int.* 23 (2016) 1722–1731, <https://doi.org/10.1007/s11356-015-5431-5>.
- [32] W. Zhai, F. Yang, D. Mao, Y. Luo, Fate and removal of various antibiotic resistance genes in typical pharmaceutical wastewater treatment systems, *Environ. Sci. Pollut. Res. Int.* 23 (2016) 12030–12038, <https://doi.org/10.1007/s11356-016-6350-9>.
- [33] J. Scaria, K.V. Anupama, P.V. Nidheesh, Tetracyclines in the environment: An overview on the occurrence, fate, toxicity, detection, removal methods, and sludge management, *Sci. Total Environ.* 771 (2021) 145291, <https://doi.org/10.1016/j.scitotenv.2021.145291>.
- [34] H. Bader, J. Hoigné, Determination of ozone in water by the indigo method, *Water Res.* 15 (1981) 449–456, [https://doi.org/10.1016/0043-1354\(81\)90054-3](https://doi.org/10.1016/0043-1354(81)90054-3).
- [35] S. Li, X. Fan, M. Gu, G. Cagnetta, J. Huang, G. Yu, Confined-space strategy for anchoring catalytic nanoparticles on Si-OH by ball milling for enhanced O₃/PMS oxidation of ciprofloxacin, *Chem. Eng. J.* 429 (2022) 132318, <https://doi.org/10.1016/j.cej.2021.132318>.
- [36] J. Liang, H. Chen, T. Mou, L. Zhang, Y. Lin, L. Yue, Y. Luo, Q. Liu, N. Li, A. Alshehri, I. Shakir, P.O. Agboola, Y. Wang, B. Tang, D. Ma, X. Sun, Coupling denitrification and ammonia synthesis via selective electrocatalytic reduction of nitric oxide over Fe₂O₃ nanorods, *J. Mater. Chem. A* 10 (2022) 6454–6462, <https://doi.org/10.1039/D2TA00744D>.
- [37] S. Li, J. Wang, Y. Ye, Y. Tang, X. Li, F. Gu, L. Li, Composite Si-O-metal network catalysts with uneven electron distribution: enhanced activity and electron transfer for catalytic ozonation of carbamazepine, *Appl. Catal. B Environ.* 263 (2020) 118311, <https://doi.org/10.1016/j.apcatb.2019.118311>.
- [38] B. Yuan, Z. Qian, X. Yang, M. Luo, X. Feng, L. Fu, W. Yang, L. Yang, J. Zhang, Y. Zhao, R. Hao, Microwave-induced deep catalytic oxidation of NO using molecular-sieve-supported oxygen-vacancy-enriched Fe–Mn bimetal oxides, *Environ. Sci. Technol.* 56 (2022) 10423–10432, <https://doi.org/10.1021/acs.est.2c02851>.
- [39] L. Xie, Q. Chen, Y. Liu, Q. Ma, J. Zhang, C. Tang, G. Duan, A. Lin, T. Zhang, S. Li, Enhanced remediation of Cr(VI)-contaminated soil by modified zero-valent iron with oxalic acid on biochar, *Sci. Total Environ.* 905 (2023) 167399, <https://doi.org/10.1016/j.scitotenv.2023.167399>.
- [40] J. Lu, H. Hao, L. Zhang, Z. Xu, L. Zhong, Y. Zhao, D. He, J. Liu, D. Chen, H. Pu, S. He, Y. Luo, The investigation of the role of basic lanthanum (La) species on the improvement of catalytic activity and stability of HZSM-5 material for eliminating methanethiol-(CH₃SH), *Appl. Catal. B Environ.* 237 (2018) 185–197, <https://doi.org/10.1016/j.apcatb.2018.05.063>.
- [41] Y. Sun, K. Xu, Z. Wei, H. Li, T. Zhang, X. Li, W. Cai, J. Ma, H.J. Fan, Y. Li, Strong electronic interaction in dual-cation-incorporated NiSe₂ nanosheets with lattice distortion for highly efficient overall water splitting, *Adv. Mater.* 30 (2018) 1802121, <https://doi.org/10.1002/adma.201802121>.
- [42] Y. Feng, W. Li, M. Meng, H. Yin, J. Mi, Mesoporous Sn(IV) doping MCM-41 supported Pd nanoparticles for enhanced selective catalytic oxidation of 1,2-propanediol to pyruvic acid, *Appl. Catal. B Environ.* 253 (2019) 111–120, <https://doi.org/10.1016/j.apcatb.2019.04.051>.
- [43] H. Jiang, J. Lin, X. Wu, W. Wang, Y. Chen, M. Zhang, Efficient hydrogenation of CO₂ to methanol over Pd/In₂O₃/SBA-15 catalysts, *J. CO₂ Util.* 36 (2020) 33–39, <https://doi.org/10.1016/j.jcou.2019.10.013>.
- [44] M. Zhang, L. Qiu, Y. Sun, Y. Song, Z. Wu, Y. Liu, Z. Yang, Y. Liu, J. Zhang, B. Zhong, X. Guo, Microstructure-controlled Li-rich Mn-based cathodes by a gas–solid interface reaction for tackling the continuous activation of Li₂MnO₃, *ACS Appl. Mater. Interfaces* 13 (2021) 40995–41003, <https://doi.org/10.1021/acsaami.1c12221>.
- [45] N. Zhang, J. Wang, Q. Li, Y. Xin, L. Zheng, Y. Wang, Z. Zhang, Enhanced selective catalytic reduction of NO with NH₃ over homoatomic dinuclear sites in defective α -Fe₂O₃, *Chem. Eng. J.* 426 (2021) 131845, <https://doi.org/10.1016/j.cej.2021.131845>.
- [46] Z. Chen, B. Lin, Y. Huang, Y. Liu, Y. Wu, R. Qu, C. Tang, Pyrolysis temperature affects the physicochemical characteristics of lanthanum-modified biochar derived from orange peels: insights into the mechanisms of tetracycline adsorption by spectroscopic analysis and theoretical calculations, *Sci. Total Environ.* 862 (2023) 160860, <https://doi.org/10.1016/j.scitotenv.2022.160860>.
- [47] K. Wang, Y. Sun, J. Tang, J. He, H. Sun, Aqueous Cr(VI) removal by a novel ball milled Fe⁰-biochar composite: role of biochar electron transfer capacity under high pyrolysis temperature, *Chemosphere* 241 (2020) 125044, <https://doi.org/10.1016/j.chemosphere.2019.125044>.
- [48] W.P. Da Silva, T.D. Carlos, G.S. Cavallini, D.H. Pereira, Peracetic acid: Structural elucidation for applications in wastewater treatment, *Water Res.* 168 (2020) 115143, <https://doi.org/10.1016/j.watres.2019.115143>.
- [49] G. Huang, C. Wang, C. Yang, P. Guo, H. Yu, Degradation of bisphenol A by peroxymonosulfate catalytically activated with Mn_{1.8}Fe_{1.2}O₄ nanospheres: synergism between Mn and Fe, *Environ. Sci. Technol.* 51 (2017) 12611–12618, <https://doi.org/10.1021/acs.est.7b03007>.
- [50] S. Xin, G. Liu, X. Ma, J. Gong, B. Ma, Q. Yan, Q. Chen, D. Ma, G. Zhang, M. Gao, Y. Xin, High efficiency heterogeneous Fenton-like catalyst biochar modified CuFeO₂ for the degradation of tetracycline: economical synthesis, catalytic performance and mechanism, *Appl. Catal. B Environ.* 280 (2021) 119386, <https://doi.org/10.1016/j.apcatb.2020.119386>.
- [51] M. McFadden, J. Loconsole, A.J. Schokling, R. Nerenberg, J.P. Pavissich, Comparing peracetic acid and hypochlorite for disinfection of combined sewer overflows: effects of suspended-solids and pH, *Sci. Total Environ.* 599–600 (2017) 533–539, <https://doi.org/10.1016/j.scitotenv.2017.04.179>.
- [52] Q. Jin, J. Kang, Q. Chen, J. Shen, F. Guo, Z. Chen, Efficiently enhanced Fenton-like reaction via Fe complex immobilized on silica particles for catalytic hydrogen peroxide degradation of 2,4-dichlorophenol, *Appl. Catal. B Environ.* 268 (2020) 118453, <https://doi.org/10.1016/j.apcatb.2019.118453>.
- [53] J. Deng, H. Wang, Y. Fu, Y. Liu, Phosphate-induced activation of peracetic acid for diclofenac degradation: kinetics, influence factors and mechanism, *Chemosphere* 287 (2022) 132396, <https://doi.org/10.1016/j.chemosphere.2021.132396>.
- [54] Y. Wang, G. Yu, Challenges and pitfalls in the investigation of the catalytic ozonation mechanism: a critical review, *J. Hazard. Mater.* 436 (2022) 129157, <https://doi.org/10.1016/j.jhazmat.2022.129157>.
- [55] Y. Chen, Y. Mu, L. Tian, L. Zheng, Y. Mei, Q. Xing, W. Liu, J. Zou, L. Yang, S. Luo, D. Wu, Targeted decomplexation of metal complexes for efficient metal recovery by ozone/percarbonate, *Environ. Sci. Technol.* 57 (2023) 5034–5045, <https://doi.org/10.1021/acs.est.3c00190>.
- [56] F. Miao, X. Yue, C. Cheng, X. Chen, W. Ren, H. Zhang, Insights into the mechanism of carbocatalysis for peracetic acid activation: kinetic discernment and active site identification, *Water Res.* 227 (2022) 119346, <https://doi.org/10.1016/j.watres.2022.119346>.
- [57] Y. Zou, J. Li, J. Tan, L. Lyu, S. Li, Y. Wang, Y. Lu, X. Zhu, T. Zhang, High-valent cobalt-oxo species triggers singlet oxygen for rapid contaminants degradation along with mild peroxymonosulfate decomposition in single Co atom-doped g-C₃N₄, *Chem. Eng. J.* 471 (2023) 144531, <https://doi.org/10.1016/j.cej.2023.144531>.
- [58] M. Xu, Efficient catalytic ozonation over Co-ZFO@Mn-CN for oxalic acid degradation: synergistic effect of oxygen vacancies and HOO-Mn-N_x bonds, *Appl. Catal. B Environ.* 322 (2023) 122085, <https://doi.org/10.1016/j.apcatb.2022.122085>.
- [59] J. Song, N. Hou, X. Liu, M. Antonietti, Y. Wang, Y. Mu, Unsaturated single-atom CoN₃ sites for improved Fenton-like reaction towards high-valent metal species, *Appl. Catal. B Environ.* 325 (2023) 122368, <https://doi.org/10.1016/j.apcatb.2023.122368>.
- [60] W. Qu, Z. Tang, S. Tang, H. Wen, J. Fang, Q. Lian, D. Shu, C. He, Cation substitution induced d-band center modulation on Cobalt-based spinel oxides for catalytic ozonation, *Adv. Funct. Mater.* 33 (2023) 2301677, <https://doi.org/10.1002/adfm.202301677>.
- [61] T. Ren, M. Yin, S. Chen, C. Ouyang, X. Huang, X. Zhang, Single-atom Fe-N₄ sites for catalytic ozonation to selectively induce a nonradical pathway toward wastewater purification, *Environ. Sci. Technol.* 57 (2023) 3623–3633, <https://doi.org/10.1021/acs.est.2c07653>.
- [62] C. Cai, X. Duan, X. Xie, S. Kang, C. Liao, J. Dong, Y. Liu, S. Xiang, D.D. Dionysiou, Efficient degradation of clofibric acid by heterogeneous catalytic ozonation using CoFe₂O₄ catalyst in water, *J. Hazard. Mater.* 410 (2021) 124604, <https://doi.org/10.1016/j.jhazmat.2020.124604>.
- [63] Y. Liu, H. Zhou, C. Jin, C. Tang, W. Zhang, G. Liu, L. Zhu, F. Chu, Z. Kong, Bio-porphyrin supported single-atom iron catalyst boosting peroxymonosulfate activation for pollutants degradation: a singlet oxygen-dominated nonradical

- pathway, *Appl. Catal. B Environ.* 338 (2023) 123061, <https://doi.org/10.1016/j.apcatb.2023.123061>.
- [64] Y. Gao, Y. Zhu, T. Li, Z. Chen, Q. Jiang, Q. Jiang, Z. Zhao, X. Liang, C. Hu, Unraveling the high-activity origin of single-atom iron catalysts for organic pollutant oxidation via peroxymonosulfate activation, *Environ. Sci. Technol.* 55 (2021) 8318–8328, <https://doi.org/10.1021/acs.est.1c01131>.
- [65] D. Ma, J. Cao, K. Liu, Y. Zhang, Q. Liang, Y. Huang, X. Guan, L. Hu, C. He, D. Xia, Interstitial carbon-platinum electronic metal-support interaction structure boost synergistic removal of O₃ and CH₃SH via surface atomic oxygen, *Appl. Catal. B Environ.* 329 (2023) 122578, <https://doi.org/10.1016/j.apcatb.2023.122578>.
- [66] Y. Cheng, B. Wang, P. Yan, J. Shen, J. Kang, S. Zhao, X. Zhu, L. Shen, S. Wang, Y. Shen, Z. Chen, In-situ formation of surface reactive oxygen species on defective sites over N-doped biochar in catalytic ozonation, *Chem. Eng. J.* 454 (2023) 140232, <https://doi.org/10.1016/j.cej.2022.140232>.
- [67] B. Huang, Z. Wu, X. Wang, X. Song, H. Zhou, H. Zhang, P. Zhou, W. Liu, Z. Xiong, B. Lai, Coupled surface-confinement effect and pore engineering in a single-Fe-atom catalyst for ultrafast Fenton-like reaction with high-valent iron-oxo complex oxidation, *Environ. Sci. Technol.* 57 (2023) 15667–15679, <https://doi.org/10.1021/acs.est.3c05509>.
- [68] B. Zhang, X. Li, K. Akiyama, P.A. Bingham, S. Kubuki, Elucidating the mechanistic origin of a spin state-dependent FeN_x-C catalyst toward organic contaminant oxidation via peroxymonosulfate activation, *Environ. Sci. Technol.* 56 (2022) 1321–1330, <https://doi.org/10.1021/acs.est.1c05980>.
- [69] M.H. Khan, H. Bae, J.-Y. Jung, Tetracycline degradation by ozonation in the aqueous phase: proposed degradation intermediates and pathway, *J. Hazard. Mater.* 181 (2010) 659–665, <https://doi.org/10.1016/j.jhazmat.2010.05.063>.
- [70] J. Zhou, F. Pan, T. Wang, Y. Zhang, Q. Yao, C. Zhu, Y. Zhu, H. Ma, J. Niu, Controlled synthesis of water-soluble Pt nanoclusters and their co-catalysis with RuO₂-IrO₂ for electrochemical degradation of tetracycline, *Sep. Purif. Technol.* 295 (2022) 121323, <https://doi.org/10.1016/j.seppur.2022.121323>.
- [71] X. Chen, J. Zhou, Y. Chen, Y. Zhou, L. Ding, H. Liang, X. Li, Degradation of tetracycline hydrochloride by coupling of photocatalysis and peroxymonosulfate oxidation processes using CuO-BiVO₄ heterogeneous catalyst, *Process Saf. Environ. Prot.* 145 (2021) 364–377, <https://doi.org/10.1016/j.psep.2020.08.016>.
- [72] J. Zheng, Z. Xu, S. Xin, B. Zhu, L. Nie, Generation of singlet oxygen over CeO₂/K, Na-codoped g-C₃N₄ for tetracycline hydrochloride degradation over a wide pH range, *Dalton Trans.* 51 (2022) 12883–12894, <https://doi.org/10.1039/D2DT01748B>.
- [73] Y. Cao, K. Cui, Y. Chen, M. Cui, G. Li, D. Li, X. Yang, Efficient degradation of tetracycline by H₂O₂ catalyzed by FeOCl: a wide range of pH values from 3 to 7, *Solid State Sci.* 113 (2021) 106548, <https://doi.org/10.1016/j.solidstatesciences.2021.106548>.
- [74] Y. Xiao, Y. Jiang, E. Zhou, W. Zhang, Y. Liu, J. Zhang, X. Wu, Q. Qi, Z. Liu, In-suit fabricating an efficient electronic transport channels via S-scheme polyaniline/Cd_{0.5}Zn_{0.5}S heterojunction for rapid removal of tetracycline hydrochloride and hydrogen production, *J. Mater. Sci. Technol.* 153 (2023) 205–218, <https://doi.org/10.1016/j.jmst.2022.12.060>.